FIGURE 3. **Linker sequence between F-box and substrate-binding domains of Fbs1 hampers SCF^{Fbs1} complex formation.** *A*, schematic representation of constructs of fusion proteins consisting of Fbs1 and Fbs2 fragments. The fragments derived from Fbs1 and Fbs2 appear in *gray* and *white boxes*, respectively. The *numbers* above the constructs represent the amino acid position of Fbs1. The *vertical bars* represent identical amino acids between Fbs1 and Fbs2. P and F-box domains, linker sequence, and sugar-binding domain are represented by *P*, *F-box*, *linker*, and *SBD*, respectively. The binding activities of these constructs toward Cul1 and Skp1 shown in *B* are summarized on the *right*, with + representing strong binding, ± representing weak binding, and − representing no binding. *B*, 293T cells were transfected with plasmids encoding the FLAG-tagged mutants F-box proteins represented in *A*. Whole cell lysates were subjected to immunoprecipitation (*IP*) with an antibody to FLAG, and the resulting precipitates were analyzed by immunoblotting with antibodies to Cul1, Skp1, and FLAG. *Asterisks* show Ig heavy and light chains. *C*, 293T cells were transfected with FLAG-tagged Fbs1, Fbs-2N1C, Fbs1 I2, or Fbs2. Cell lysates were fractionated by ultracentrifugation, and FLAG-Fbs1 was immunoprecipitated with an antibody to FLAG from 100,000 × *g* supernatant (*s*) and precipitate (*p*) fractions. The resulting immunoprecipitates were analyzed by immunoblotting as in Fig. 2*B*.
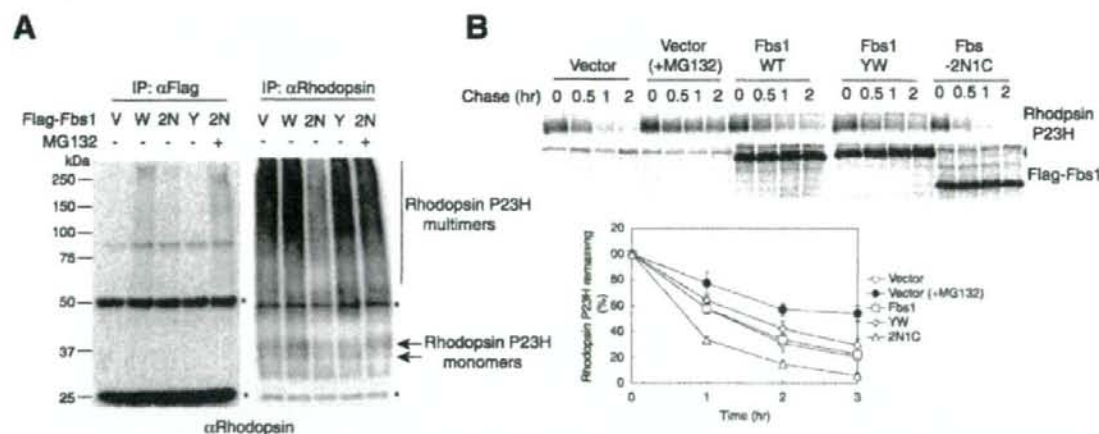

FIGURE 4. **Expression of Fbs-2N1C promotes substrate degradation.** *A*, 293T cells were transfected with plasmids encoding FLAG-tagged empty vector (*V*), Fbs1 (*W*), Fbs-2N1C (*2N*), or Fbs1 YW (*Y*) and combination with rhodopsin P23H mutant. Some cells were treated with 10 μM MG132 for 16 h. Whole cell lysates were subjected to immunoprecipitation (*IP*) with antibodies to FLAG and rhodopsin, and the resulting precipitates were analyzed by immunoblotting with an antibody to rhodopsin. *Asterisks* show Ig heavy and light chains. *B*, rhodopsin P23H was co-transfected with FLAG-tagged empty vector, Fbs1, Fbs-2N1C, or Fbs1 YW. Twenty-four hours after transfection, 293T cells were pulse-labeled with [^{35}S]Met/Cys for 1 h and chased for the indicated time intervals. Rhodopsin P23H and Fbs1 derivatives were immunoprecipitated with antibodies to rhodopsin and FLAG, respectively. The plotted data at the bottom show a quantification analysis of the stability of rhodopsin P23H over time in the *upper panels*. Data are the mean ± S.D. of three independent experiments. *WT*, wild type.

Fbs-2N1C could bind to P23H, although its binding to P23H seemed weaker than that of wild-type Fbs1 (Fig. 4*A*, *left panel*). Since the activity to bind RNaseB was not different between Fbs1 and Fbs-2N1C (data not shown), it seems likely that the SCF$^{Fbs-2N1C}$ causes degradation of P23H through its ubiquitylation. Interestingly, the quantity of P23H decreased upon Fbs-

2N1C expression (Fig. 4*A*, *right panel*). It has been reported that the degradation of P23H was suppressed by MG132 treatment (15, 16). The quantities of both P23H associated with Fbs-2N1C and the P23H protein were recovered by the addition of MG132. Moreover, we performed pulse-chase analysis using 293T cells co-expressing the P23H mutant and FLAG-tagged
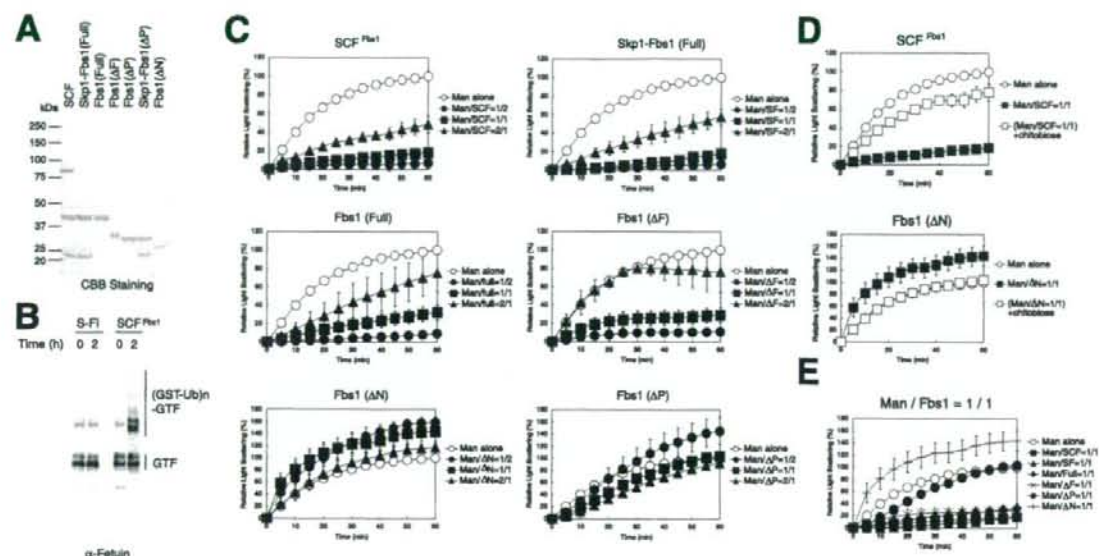
- 357 -

FIGURE 5. **Fbs1 complexes suppress the aggregation of denatured α-mannosidase in vitro.** *A,* electrophoretic pattern of the recombinant proteins produced by the baculovirus system. *CBB Staining,* Coomassie Brilliant Blue staining. *B,* GlcNAc-terminated fetuin (*GTF*) was incubated in a reaction mixture containing the ATP-regenerating system, recombinant ubiquitin-activating enzyme (E1), Ubc4, GST-ubiquitin (*GST-Ub*), and Skp1-Fbs1 dimer (*S-F1*) or SCF complex (*SCF*) in the presence of the NEDD8 system at 30 °C. The high molecular mass ubiquitylated fetuin ((*GST-Ub*)n-GTF) was detected by immunoblotting with anti-fetuin antibody. *C,* after denaturation in 6 M GdnHCl, α-mannosidase (*Man*) was diluted to a final concentration of 0.3 mM at 25 °C in the presence of the indicated concentrations of SCF[Fbs1] (*SCF[Fbs1]* or *SCF*), Skp1 and Fbs1 dimer (*Skp1-Fbs1 (Full)* or *SF*), Fbs1 monomer (*Fbs1 (Full)* or *Full*), or Fbs1 derivatives (*ΔF, ΔN,* or *ΔP*). Aggregation was measured by monitoring light scattering at 360 nm over a period of 60 min. Data are the mean ± S.D. of at least three independent experiments. *D,* α-mannosidase was allowed to aggregate in the presence of equal mole of SCF[Fbs1] or Fbs1 (ΔN). 0.05 mM N, N'-diacetylchitobiose was added (+*chitobiose*), and the effects on aggregation were monitored by measuring light scattering at 360 nm. Data are the mean and standard deviation of three independent experiments. *E,* α-mannosidase was allowed to aggregate in the presence of equal mole of recombinant Fbs1 complexes or derivatives. Data are the mean ± S.D. of three independent experiments.

Fbs1 derivatives. The degradation of P23H was suppressed by MG132 treatment as reported previously (Fig. 4*B*). Although wild-type Fbs1 or the YW mutant did not influence the kinetics of P23H degradation, co-expression of Fbs-2N1C efficiently promoted its degradation. On the other hand, like wild-type Fbs1, Fbs1 I2, could associate with P23H, but its expression did not influence both the amount of P23H and the kinetics of P23H degradation (data not shown). These results demonstrate that the non-SCF complex of Fbs1 can be converted to an active E3 ligase by introducing the complex-forming activity mapped onto the F-box domain and the linker sequence of Fbs2.

Fbs1 Suppresses Aggregation of Denatured Glycoprotein in Vitro—We reported previously that the expression of Fbs1 inhibits aggresome formation in Cos7 cells (8). Furthermore, since Fbs1 interacts with denatured glycoproteins more efficiently than native glycoproteins, we examined whether Fbs1 functions as a molecular chaperone for glycoproteins *in vitro*. To this end, we prepared recombinant SCF[Fbs1], Skp1-Fbs1 dimers, Fbs1, Fbs1 ΔF, Fbs1 ΔP, Skp1-ΔP dimers, and Fbs1 ΔN, all of which were produced by using a baculovirus system (Fig. 5*A*). To obtain highly purified recombinant proteins, we purified them by using the affinity for the RNaseB resin but not nickel resin toward His tag. The purified SCF[Fbs1] but not Skp1-Fbs1 dimers could ubiquitylate GlcNAc-terminated fetuin (*GTF*) effectively (Fig. 5*B*). We next assessed the ability of these proteins or their complexes to suppress the aggregation by

using denatured α-mannosidase that contains high mannose type oligosaccharides, a typical substrate for the glycoprotein aggregation assay (17). Although Fbs1 alone suppressed the aggregation of denatured α-mannosidase in a concentration-dependent manner, the Fbs1-Skp1 dimers as well as the SCF[Fbs1] complex suppressed the aggregation much more effectively than Fbs1 alone (Fig. 5*C*). Although the addition of half-molar of Fbs1 ΔF did not affect the aggregation of denatured α-mannosidase, ΔF was also active to suppress the aggregation at a level similar to that of Fbs1 alone in an equal molar ratio, suggesting that the partial suppression by Fbs1 is independent of the hydrophobic F-box domain. On the other hand, ΔN, consisting of substrate-binding domain alone, enhanced its aggregation. Both the aggregation-suppressing activity of SCF[Fbs1], Skp1-Fbs1 dimers, or Fbs1 and the aggregation-enhancing activity of ΔN were inhibited by chitobiose (Fig. 5*D* and not shown). In contrast, these recombinant Fbs1 protein complexes had no effect on the aggregation of non-glycosylated proteins such as citrate synthase and luciferase (data not shown). Importantly, ΔP as well as the Skp1-ΔP dimers could not suppress the aggregation of α-mannosidase in an equal molar ratio (Fig. 5, *C* and *E*, and not shown). These results indicate that the Skp1-Fbs1 dimers effectively suppress the aggregation of denatured glycoproteins by recognizing the exposed chitobiose in *N*-glycans and that the P domain of Fbs1 is required for this aggregation suppressing activity.

DISCUSSION

The F-box family of proteins, which are the substrate-recognition subunits of the SCF ubiquitin ligase, play important roles in ubiquitin-dependent proteolysis in eukaryotes (18, 19). However, it is not clear whether all F-box proteins indeed function as receptor subunits of SCF complexes. For example, it has been reported that at least two F-box proteins, Ctfl3 and Rcy1, out of 11 F-box proteins in *Saccharomyces cerevisiae*, do not form SCF complexes (20–22). Since not all RING-finger proteins are ubiquitin ligases, it is possible that non-canonical F-box proteins that fail to form the SCF complex play some important roles other than ubiquitin ligase activity. In the present study, we showed that the SCF complex formation of Fbs1, which recognizes *N*-glycans, is not efficient and that the intervening segment between the F-box domain and the sugar-binding domain of Fbs1 suppresses the formation of the SCF complex. The major population of Fbs1 is present as Fbs1-Skp1 heterodimers or Fbs1 monomers, which can inhibit the aggregation of the glycoproteins. Our results show that Fbs1 contributes to a chaperone function in addition to the role of the SCF[Fbs1] ubiquitin ligase, opening new perspectives for cellular activities of F-box proteins.

Although most endogenous Fbs1 was not assembled into the SCF[Fbs1] complex, a minor population of Fbs1 was capable of forming the SCF[Fbs1] complex in cells. Moreover, the SCF[Fbs1] complex could be produced in insect cells by infection with the baculovirus, indicating that Fbs1 can intrinsically form the SCF complex. It is worth noting that the SCF[Fbs1] was mainly present in the $100,000 \times g$ precipitate fraction including the microsome (Fig. 2, *B* and *C*). It is not clear why the SCF[Fbs1] is bound to the ER membrane, although it is plausible that it plays a pivotal role in the ERAD pathway. To examine how the SCF complex formation of Fbs1 was promoted *in vivo*, we treated Fbs1-expressing cells with ER stress inducers, such as thapsigargin and dithiothreitol or a proteasome inhibitor MG132. These treatments, however, did not affect the SCF complex formation (data not shown). Furthermore, although the interaction between Fbs1 and its substrate glycoproteins did not affect the SCF complex formation (Figs. 1*A* and 3*B*), we examined the effects of overexpression of p97/VCP, Fbs1 substrates, Skp1, or Cul1. No protein other than Cul1 accelerated the SCF[Fbs1] formation not only in the $100,000 \times g$ precipitate fraction but also in the cytosol (Fig. 2*A* and data not shown). Intriguingly, whereas Fbs1 and Skp1 were mainly located in the cytosol ($100,000 \times g$ supernatant fraction), Cul1 was detected not only in the cytosol but also in the $100,000 \times g$ precipitate fraction (Figs. 2, *B* and *C*, and 3*C*), suggesting that Cul1 is recruited to the microsome membrane where the SCF[Fbs1] complex will be assembled to ubiquitylate efficiently the *N*-linked glycosylated ERAD substrates.

Fbs1 belongs to a subfamily consisting of at least five homologous F-box proteins that contain a conserved FBA motif in their C termini (5, 6). Among them, at least Fbs2 recognizes high mannose oligosaccharides as well as Fbs1 and forms an SCF-type ubiquitin ligase. The Fbs1 protein sequence shows highly homologous to that of Fbs2 other than the P domain of Fbs1 and C-terminal part of Fbs2, but the linker sequence

between the F-box and FBA domains shows lower homology than other portions (Fig. 3*A*). As shown in Fig. 3*B*, the difference in the ability for assembling into the SCF complex between Fbs1 and Fbs2 is ascribed to the short linker sequence (92–117 amino acids of Fbs1). Although Fbs2 formed the SCF complex efficiently in the cytosol as well as the $100,000 \times g$ precipitate fraction, the SCF[Fbs1] formation was mainly present bound on the ER membrane (Fig. 3*C*). Although it is not clear whether the linker sequence of Fbs1 prevents the SCF[Fbs1] from being in the cytosol or causes the formation of the SCF[Fbs1] bound on the ER membrane, this limited localization of SCF[Fbs1] is also due to the linker sequence (Fig. 3*C*). Crystal structure and mutational analyses of Cdc4 and βTrCP1 revealed the importance of orientation and rigidity in the linker sequence between F-box and WD40 domains for their *in vivo* function (23, 24). The linker sequences of Cdc4 and βTrCP1 are longer than that of Fbs1 and form three or four helix globular domains. On the other hand, the linker sequence of Fbs1 is an unstructured domain that consists of a flexible linker loop and an α-helix and is too far from Cul1 to influence directly the SCF complex formation.[3] The information of the structure of Skp1-Fbs1 suggests that the prevention of the SCF complex formation by this unstructured linker sequence can be cancelled by binding to the membrane or unidentified proteins on the ER.

In this study, we demonstrated that the Fbs1 could suppress the aggregation of denatured glycoproteins. This activity is due to the N-terminal P domain that is not seen in other F-box proteins. This N-terminal domain has been reported as a PEST sequence rich in proline, glutamic acid, serine, and threonine, which are often found in short-lived proteins (25). The N-terminal sequence in Fbs1, however, did not seem to act as a general PEST because the deletion of the P domain from Fbs1 or the addition to Fbs2 did not affect the protein stability (Fig. 3). More recently, it has been reported that U-box type E3 CHIP (C terminus of Hsc-70-interacting protein) is associated with Fbs1 through the P domain (26). Although we did not detect the E3 activity of the Skp1-Fbs1 dimers produced in the insect cells toward glycoprotein substrate GlcNAc-terminated fetuin (Fig. 5*B*), it is possible that an unknown chaperone molecule of insect cells was bound to the P domain of Fbs1. Skp1-Fbs1 dimers and Fbs1 monomers as well as the SCF[Fbs1] complex showed activity to suppress the denatured glycoprotein aggregation, suggesting that the majority of Fbs1 is present as Skp1-Fbs1 dimers or Fbs1 monomers in cells and is not an intermediate prior to assembly of the SCF[Fbs1] complex, but rather, a novel functional unit.

It is predicted that more than 30% of eukaryotic proteins contain substantial regions of disordered structure (27). One feature of intrinsically disordered proteins is their rapid degradation. Intracellular protein quality control, especially the degradation of proteins with aberrant structures, is thought to be important particularly in quiescent cells such as neurons (28). Fbs1 is expressed mainly in neuronal cells in the adult brain (14). Recently, it has been reported (29, 30) that loss of autophagy leads to neurodegeneration even in the absence of any

---

[3] Mizushima, T., Yoshida, Y., Kumanomidou, T., Hasegawa, Y., Suzuki, A., Yamane, T., and Tanaka, K., unpublished data.

aggregation-prone mutant proteins. Moreover, these reports have shown that the primary role of autophagy under normal conditions is the turnover of diffused cytosolic proteins, rather than direct elimination of inclusion bodies (29, 30). Our study suggests that Fbs1 contributes to the clearance of such cytosolic proteins by constitutive autophagy, like other chaperone systems, to suppress the aggregation of abnormal glycoproteins in neurons. For this, the N-terminal unique sequence of Fbs1, the P domain, having chaperone function, may have been made up during evolution. Since Cul1 is a common component of the SCF complexes and Fbs1 is abundant in neuronal cells, Fbs1 may also evolutionally acquire the linker sequence that suppresses the SCF^{Fbs1} complex formation to supply Cul1 toward other F-box proteins. It also seems possible that Fbs1 functions as a chaperone to keep the solubility of a particular glycoprotein(s) in the cytosol in neuronal cells. Further studies are needed to identify the Fbs1 target glycoproteins in neuronal cells, which may reveal the role of Fbs1 in maintaining homeostasis of neuronal cells.

REFERENCES

1. Feldman, R. M., Correll, C. C., Kaplan, K. B., and Deshaies, R. J. (1997) *Cell* **91,** 221–230
2. Skowyra, D., Craig, K. L., Tyers, M., Elledge, S. J., and Harper, J. W. (1997) *Cell* **91,** 209–219
3. Bai, C., Sen, P., Hofmann, K., Ma, L., Goebl, M., Harper, J. W., and Elledge, S. J. (1996) *Cell* **86,** 263–274
4. Jin, J., Cardozo, T., Lovering, R. C., Elledge, S. J., Pagano, M., and Harper, J. W. (2004) *Genes Dev.* **18,** 2573–2580
5. Ilyin, G. P., Serandour, A. L., Pigeon, C., Rialland, M., Glaise, D., and Guguen-Guillouzo, C. (2002) *Gene (Amst.)* **296,** 11–20
6. Winston, J. T., Koepp, D. M., Zhu, C., Elledge, S. J., and Harper, J. W. (1999) *Curr. Biol.* **9,** 1180–1182
7. Yoshida, Y., Tokunaga, F., Chiba, T., Iwai, K., Tanaka, K., and Tai, T. (2003) *J. Biol. Chem.* **278,** 43877–43884
8. Yoshida, Y., Chiba, T., Tokunaga, F., Kawasaki, H., Iwai, K., Suzuki, T., Ito, Y., Matsuoka, K., Yoshida, M., Tanaka, K., and Tai, T. (2002) *Nature* **418,** 438–442
9. Mizushima, T., Hirao, T., Yoshida, Y., Lee, S. J., Chiba, T., Iwai, K., Yamaguchi, Y., Kato, K., Tsukihara, T., and Tanaka, K. (2004) *Nat. Struct. Mol. Biol.* **11,** 365–370
10. Yoshida, Y. (2005) *Methods Enzymol.* **398,** 159–169
11. Yoshida, Y., Adachi, E., Fukiya, K., Iwai, K., and Tanaka, K. (2005) *EMBO Rep.* **6,** 239–244
12. Tanahashi, N., Murakami, Y., Minami, Y., Shimbara, N., Hendil, K. B., and Tanaka, K. (2000) *J. Biol. Chem.* **275,** 14336–14345
13. Paquet, M. E., Leach, M. R., and Williams, D. B. (2005) *Methods (Oxf.)* **35,** 338–347
14. Erhardt, J. A., Hynicka, W., DiBenedetto, A., Shen, N., Stone, N., Paulson, H., and Pittman, R. N. (1998) *J. Biol. Chem.* **273,** 35222–35227
15. Illing, M. E., Rajan, R. S., Bence, N. F., and Kopito, R. R. (2002) *J. Biol. Chem.* **277,** 34150–34160
16. Saliba, R. S., Munro, P. M., Luthert, P. J., and Cheetham, M. E. (2002) *J. Cell Sci.* **115,** 2907–2918
17. Stronge, V. S., Saito, Y., Ihara, Y., and Williams, D. B. (2001) *J. Biol. Chem.* **276,** 39779–39787
18. Cardozo, T., and Pagano, M. (2004) *Nat. Rev. Mol. Cell. Biol.* **5,** 739–751
19. Petroski, M. D., and Deshaies, R. J. (2005) *Nat. Rev. Mol. Cell. Biol.* **6,** 9–20
20. Galan, J. M., Wiederkehr, A., Seol, J. H., Haguenauer-Tsapis, R., Deshaies, R. J., Riezman, H., and Peter, M. (2001) *Mol. Cell. Biol.* **21,** 3105–3117
21. Kaplan, K. B., Hyman, A. A., and Sorger, P. K. (1997) *Cell* **91,** 491–500
22. Russell, I. D., Grancell, A. S., and Sorger, P. K. (1999) *J. Cell Biol.* **145,** 933–950
23. Orlicky, S., Tang, X., Willems, A., Tyers, M., and Sicheri, F. (2003) *Cell* **112,** 243–256
24. Wu, G., Xu, G., Schulman, B. A., Jeffrey, P. D., Harper, J. W., and Pavletich, N. P. (2003) *Mol. Cell* **11,** 1445–1456
25. Rechsteiner, M., and Rogers, S. W. (1996) *Trends Biochem. Sci.* **21,** 267–271
26. Nelson, R. F., Glenn, K. A., Miller, V. M., Wen, H., and Paulson, H. L. (2006) *J. Biol. Chem.* **281,** 20242–20251
27. Fink, A. L. (2005) *Curr. Opin. Struct. Biol.* **15,** 35–41
28. Forman, M. S., Trojanowski, J. Q., and Lee, V. M. (2004) *Nat. Med.* **10,** 1055–1063
29. Hara, T., Nakamura, K., Matsui, M., Yamamoto, A., Nakahara, Y., Suzuki-Migishima, R., Yokoyama, M., Mishima, K., Saito, I., Okano, H., and Mizushima, N. (2006) *Nature* **441,** 885–889
30. Komatsu, M., Waguri, S., Chiba, T., Murata, S., Iwata, J., Tanida, I., Ueno, T., Koike, M., Uchiyama, Y., Kominami, E., and Tanaka, K. (2006) *Nature* **441,** 880–888

- 360 -

Structural basis for the selection of glycosylated substrates by SCF^{Fbs1} ubiquitin ligase

Tsunehiro Mizushima*[†], Yukiko Yoshida[‡], Taichi Kumanomidou*, Yuko Hasegawa*, Atsuo Suzuki*, Takashi Yamane*[§], and Keiji Tanaka[‡§]

*Department of Biotechnology, Graduate School of Engineering, Nagoya University, Chikusa-ku, Nagoya 464-8603, Japan; [†]Precursor Research for Embryonic Science and Technology, Japan Science and Technology Agency, Kawaguchi, Saitama 332-0012, Japan; and [‡]Laboratory of Frontier Science, Tokyo Metropolitan Institute of Medical Science, Bunkyo-ku, Tokyo 113-8613, Japan
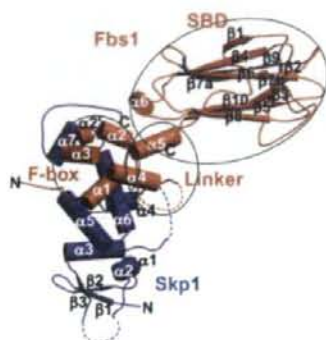
The ubiquitin ligase complex SCF^{Fbs1}, which contributes to the ubiquitination of glycoproteins, is involved in the endoplasmic reticulum-associated degradation pathway. In SCF ubiquitin ligases, a diverse array of F-box proteins confers substrate specificity. Fbs1/Fbx2, a member of the F-box protein family, recognizes high-mannose oligosaccharides. To elucidate the structural basis of SCF^{Fbs1} function, we determined the crystal structures of the Skp1–Fbs1 complex and the sugar-binding domain (SBD) of the Fbs1–glycoprotein complex. The mechanistic model indicated by the structures appears to be well conserved among the SCF ubiquitin ligases. The structure of the SBD–glycoprotein complex indicates that the SBD primarily recognizes Man$_3$GlcNAc$_2$, thereby explaining the broad activity of the enzyme against various glycoproteins. Comparison of two crystal structures of the Skp1–Fbs1 complex revealed the relative motion of a linker segment between the F-box and the SBD domains, which might underlie the ability of the complex to recognize different acceptor lysine residues for ubiquitination.

glycoprotein | tertiary structure | ubiquitin system

Fig. 1. Structure of the Skp1–Fbs1 complex. Skp1 and Fbs1 are colored blue and red, respectively. The secondary structure elements for Skp1 and Fbs1 are labeled. Dotted lines represent disordered regions. The F-box, linker, and SBD domains of Fbs1 are circled.

U biquitin-mediated proteolysis plays a regulatory role in a number of diverse cellular processes and involves the selective destruction of short-lived functional proteins (1). The ubiquitin–proteasome system also is responsible for the disposal of misfolded and unfolded cellular proteins, the aberrant accumulation of which usually causes cell death, which can lead to neurodegenerative diseases (2). Protein ubiquitination is catalyzed by a sophisticated cascade system consisting of the ubiquitin-activating (E1), ubiquitin-conjugating (E2), and ubiquitin-ligating (E3) enzymes (3). Among these enzymes, the E3 enzymes are responsible for the selection of target proteins. E3 enzymes are a diverse family of proteins and protein complexes. One of the best characterized groups of E3 enzymes is the SCF complex [composed of Skp1, Cul1, Rbx1 (also called Roc1), and an F-box protein], which regulates the degradation of a broad range of cellular proteins (4). F-box proteins consist of an N-terminal ≈40-aa F-box domain that binds to Skp1 and various C-terminal substrate-recognition regions and are subcategorized into three classes according to their substrate-binding domains. The Fbw (or FBXW) and Fbl (or FBXL) families possess WD40 repeats and leucine-rich repeats in their binding domains, respectively (5). The third class of F-box proteins is the Fbx (or FBXO) family, which does not contain any presumptive functional domains. However, we recently identified a subfamily within the Fbx family that consists of at least five homologous F-box proteins that recognize N-glycan; we named the sugar-binding domain (SBD)-containing proteins of this subfamily the Fbs (F-box protein that recognizes sugar chains; known previously as FBG) proteins (6).

In the SCF complex, Cul1 functions as a molecular scaffold that simultaneously interacts through its N and C termini with the crucial adaptor subunits Skp1 and Rbx1 together with a specific E2 enzyme, res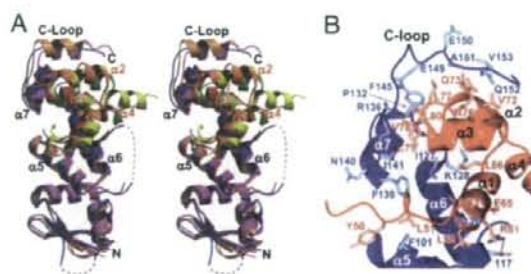pectively. Skp1 is an adaptor protein that links Cul1 and one of the F-box proteins (6). Fbw and Fbl proteins usually recognize the phosphorylation status of the substrate, and structural models of the SCF complexes of some of these proteins, such as Fbw1/β-TrCP1 (7), Fbw7/Cdc4 (8), and Fbl1/Skp2 (9–11), have been reported. Structural information, however, is available only for the recognition of phosphorylated protein substrates.

N-linked glycosylation of proteins takes place in the endoplasmic reticulum and plays a key role in protein quality control (12). Misfolded proteins and unassembled protein complexes that fail to assume their functional states in the endoplasmic reticulum are subjected to endoplasmic reticulum-associated degradation, which involves retrotranslocation into the cytosol and degradation by the ubiquitin–proteasome system. SCF^{Fbs1} is an N-linked glycoprotein-specific ubiquitin ligase complex that contains the neuron-specific F-box protein Fbs1/Fbx2/NFB42 (13–16). We previously reported x-ray crystal structures of the Fbs1 SBD alone and in complex with di-N-acetylchitobiose (chitobiose, GlcNAc-GlcNAc, or GlcNAc$_2$), which revealed that the binding site is formed by a small hydrophobic pocket located at the top of a β-sandwich (17). The molecular mechanism

Fig. 2. Structure of the Skp1–Fbs1 interface. (*A*) Stereo views of the Fbs1 F-box domain (red) and Skp1 (blue) are compared with the structures of Skp1–Skp2 and Skp1–β-TrCP1. Skp1 is purple, Skp2 is green, Skp1 is orange, and β-TrCP1 is yellow. The secondary structure elements for Skp1 and Fbs1 are labeled with black and red letters, respectively. (*B*) Close-up view of the interface between Skp1 and Fbs1 showing intermolecular contacts. Fbs1 is red and Skp1 is blue.

underlying the ubiquitination of N-glycoproteins by the SCF[Fbs1] ubiquitin ligase, however, is unknown at present. To understand the mechanistic details of the SCF[Fbs1]-mediated ubiquitination reaction, we determined the crystal structures of the SBD–glycoprotein and Skp1–Fbs1 complexes.

Results

Overall Structure of the Skp1–Fbs1 Complex. The Skp1–Fbs1 complex has an overall L-shaped structure with Skp1 and the Fbs1 subunits oriented ≈90° to each other (Fig. 1). Skp1 and the chitobiose-binding site (17) are located at the opposite ends of

Fbs1. Fbs1 consists of four distinct domains: the PEST domain (residues 1–54), the F-box domain (residues 55–95), a linker domain (residues 96–124), and the SBD (residues 125–297). The electron densities of the N-terminal PEST domain (residues 1–47) and part of the linker domain (residues 104–108) are not visible, suggesting that these regions are flexible. Although the Skp1–Fbs1 complex was crystallized in the presence of 30 mM chitobiose, the chitobiose molecule is not visible in this structure. The F-box domain comprises four α helices, which is the same structural motif observed in the Skp1-binding domains of Skp2 and β-TrCP1 (Fig. 2*A*). The SBD in the Skp1–Fbs1 complex is composed of a 10-stranded antiparallel β-sandwich, and it can be superposed on the previously reported structure of SBD alone with an average rms deviation of 0.39 Å for the Cα atoms, indicating that the structures are very similar. On the other hand, the C-terminal linker helix α5 assumes slightly different positions in the two structures because of crystal packing and the flexibility of the linker domain, which consists of α5 and a loop structure.

The Skp1 in the Skp1–Fbs1 complex adopts the same BTB/POZ fold (18) observed in previously reported structures of Skp1 (7–9). Interestingly, the C-terminal α-helix α8 of previously reported structures of Skp1 complexed with other F-box proteins is replaced with an extended structure (C loop: residues 146–155) (Fig. 2*A*). The differences in the secondary structure of Skp1 may reflect different roles of the protein. With the exception of the C-terminal loop, the overall structure of Skp1 is almost identical to those of the protein in the Skp1–Skp2 and Skp1–β-TrCP1 complexes (rms deviations for the Cα atoms: 1.8 and 2.1 Å, respectively).

Skp1–F-Box Interface. Whereas the F-box domain of Fbs1 contains the same four-helix (α1–α4) structure seen in the domains of
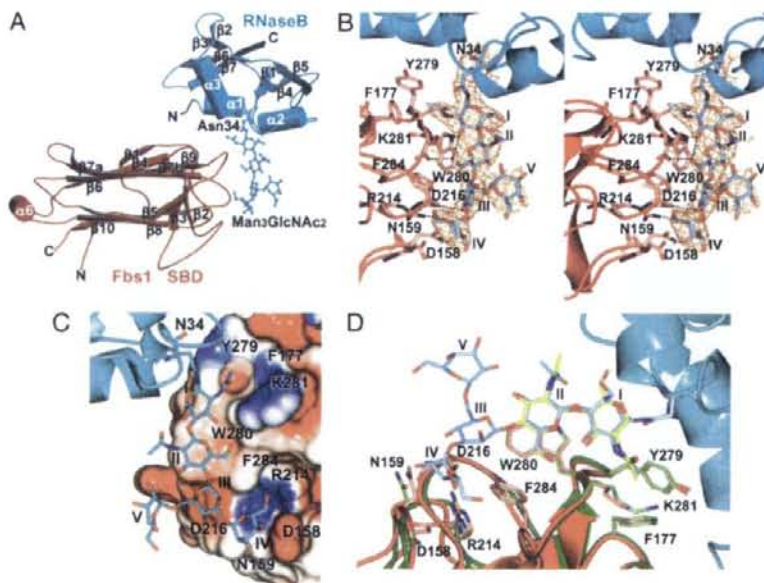

Fig. 3. Structure of the SBD–RNaseB complex. (*A*) The SBD is red and RNaseB is cyan. The secondary structure elements of the SBD and RNaseB are labeled. (*B*) Stereo view of the interface between the substrate-binding pocket of the SBD and the sugar of RNaseB. The Man3GlcNAc2 was modeled with the electron density map (2F$_o$ – F$_c$ omit map of Man3GlcNAc2) contoured at 1.1 rms deviation. Fbs1 is red and RNaseB is cyan. (*C*) Surface representation of the substrate-binding pocket of the SBD bound to Man3GlcNAc2. The surface is colored according to the electrostatic potential of the residues (blue, positive; red, negative). (*D*) Comparison between the substrate-binding sites of the Fbs1 SBD (green) bound to chitobiose (yellow) and the Fbs1 SBD (red) bound to glycosylated RNaseB (cyan).
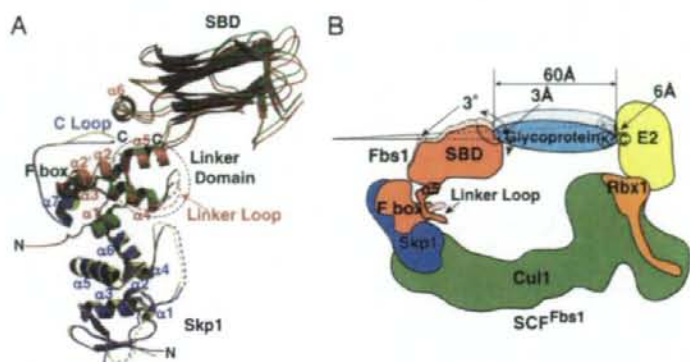
Mizushima et al.

Fig. 4. Regulatory mechanism of SCF[Fbs1] glycoprotein ubiquitination. (A) Comparison of the two crystal structures of the Skp1–Fbs1 complex. Skp1 (form 1), Fbs1 (form 1), Skp1 (form 2), and Fbs1 (form 2) are blue, red, yellow, and green, respectively. (B) Schematic representation of the model for ubiquitination on SCF[Fbs1]. The E2 active-site cysteine and acceptor lysine residues are depicted with circled letters.

Skp2 (1.5-Å rms deviation for 27 C$^\alpha$ atoms) and β-TrCP1 (1.7-Å rms deviation for 28 C$^\alpha$ atoms), there are several differences. Helix α2 in Fbs1 is composed of two segments (α2 and α2') separated by a turn, which causes it to bulge into the C loop of Skp1. The orientations of helices α3 and α4 of Fbs1 are similar to those of Skp2 but not to those of β-TrCP1 (Fig. 2A). Moreover, whereas the C-terminal region of the F-box domain of Skp2 is a loop structure, those of Fbs1 and β-TrCP1 form α-helices (α4).

The binding mode between Skp1 and the F-box domain of Fbs1 is almost identical to those between Skp1 and Skp2 (1.0-Å rms deviation for 120 C$^\alpha$ atoms) and between Skp1 and β-TrCP1 (1.1-Å rms deviation for 117 C$^\alpha$ atoms), except that the C loop of Skp1 interacts with the F-box domain through van der Waals contacts (Phe-145, Glu-149, Glu-150, Ala-151, Gln-152, and Val-153 of Skp1 interact with Val-72, Gln-73, Arg-76, Leu-77, and Leu-80 of Fbs1) (Fig. 2B). The positions of the Fbs1 F-box domain and α7 in Skp1 are shifted away from the N-terminal domain of Skp1 by ≈4.0 Å (Skp1–Skp2) or ≈2.5 Å (Skp1–β-TrCP1). These differences in the distances from the F-box domains to α7 of Skp1 and the C-terminal structures of Skp1 are likely due to the F-box structure.

Structure of the Glycoprotein Complex of the SBD. Ribonuclease B (RNaseB) is a glycoprotein that has a single high-mannose
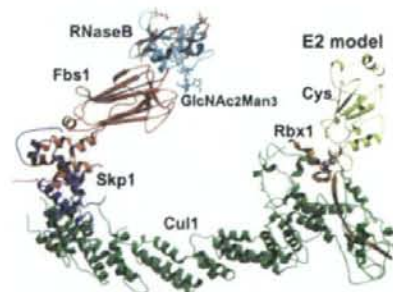

Fig. 5. Model of the SCF[Fbs1]–RNaseB complex bound to E2. Cul1, Rbx1, Skp1, Fbs1, RNaseB, and E2 are green, orange, blue, red, cyan, and yellow, respectively. Lysine residues on the RNaseB surface are presented in ball-and-stick format and are coral.

oligosaccharide (Man$_{6-8}$GlcNAc$_2$) attached at Asn-34 (19). RNaseB binds to the edge of the β-sandwich of the SBD (Fig. 3A). Clear electron density demonstrates the presence of Man$_3$GlcNAc$_2$ bound to the Fbs1 monomer, but the outer branches of the carbohydrate are disordered and not visible in the electron density map. The structure of the Fbs1-bound RNaseB, which consists of three α-helices and seven β-strands, is essentially identical to the previously reported structures of apo-RNaseB (20, 21); these structures have an average 0.59-Å rms deviation for the C$^\alpha$ positions. Similarly, the SBDs in the structures of the Skp1–Fbs1 and SBD–RNaseB complexes can be superposed with an average 0.48-Å rms deviation for the C$^\alpha$ positions, indicating that RNaseB binding does not cause any significant structural changes in the SBD.

Glycoprotein Recognition by the SBD in the SBD–RNaseB Complex. The sugar-binding surface consists of the four loops between β2 and β3, β3 and β4, β5 and β6, and β9 and β10. Man$_3$GlcNAc$_2$ interacts with nine Fbs1 residues (Asp-158, Asn-159, Phe-177, Arg-214, Asp-216, Tyr-279, Trp-280, Lys-281, and Phe-284) through hydrogen bonds and/or van der Waals contacts (Fig. 3 B and C). The molecular recognition mechanism between the chitobiose moiety and the amino acid residues in Fbs1 is similar to that reported previously for the SBD–chitobiose complex (17). The methyl group of the N-acetyl moiety from the GlcNAc (I) residue is inserted into a small hydrophobic pocket surrounded by the side chains of Phe-177, Tyr-279, and Lys-281; and the O3 atom forms a hydrogen bond with the main chain N atom of Lys-281. The GlcNAc (II) residue is stacked on the aromatic ring of Trp-280 and the O6 atom forms a hydrogen bond with the carbonyl oxygen atom of Lys-281. The two GlcNAc residues form an intramolecular hydrogen bond between the O3 atom of GlcNAc (I) and the O6 atom of GlcNAc (II). Formation of these hydrogen bonds fixes the orientation of the β(1→4)-linked GlcNAc residues. Comparison of the SBD–RNaseB complex and the previously reported SBD–chitobiose complex reveals that the substrate binding pockets (Phe-177, Tyr-279, Trp-280, and Lys-281) and the chitobiose structures can be superposed with an average rms deviation of 0.69 Å for all of the atoms (Fig. 3D). Only the side chain of Lys-281 has a different conformation, and it has been shown that Lys-281 is not essential for the binding to chitobiose (17). The outer mannose-binding residues of the SBD also do not exhibit significant conformational changes. We have reported that Fbs1 recognizes not only chitobiose but also the outer mannose branches (17). The O4 atom of Man(III)

BIOCHEMISTRY

Table 1. Data collection, phasing, and refinement statistics

	Skp1–Fbs1	Skp1–Fbs1/Thimerosal	Skp1–Fbs1	SBD–RNaseB
Data collection				
Space group	$P3_221$	$P3_221$	$P2_12_12_1$	$P432$
Cell parameters, Å				
a	106.7	106.6	66.2	148.6
b	106.7	106.6	111.1	148.6
c	110.2	113.7	153.3	148.6
Unique reflections	27,964	17,765	12,269	15,839
Resolution range, Å	2.40 (2.49–2.40)	2.80 (2.90–2.80)	3.50 (3.63–3.50)	2.70 (2.80–2.70)
R_{merge}	0.045 (0.327)	0.058 (0.328)	0.103 (0.225)	0.078 (0.325)
$I/\sigma I$	18.1 (2.7)	16.0 (2.2)	7.0 (4.1)	13.9 (5.2)
Completeness, %	97.7 (93.0)	95.7 (79.6)	85.2 (79.0)	99.4 (97.9)
Redundancy	5.4 (2.9)	6.2 (2.3)	2.6 (2.1)	11.8 (6.4)
Refinement				
No. of reflections	26,521		12,279	15,049
R_{work}/R_{free}	0.233/0.291		0.223/0.299	0.216/0.288
rms deviations				
Bond lengths, Å	0.010		0.022	0.026
Bond angles, °	1.33		2.08	2.51

Values in parentheses represent the highest-resolution shell.

forms a hydrogen bond with the sidechain O^δ atom of the Asp-216 sidechain; this hydrogen bond stabilizes the complex with the Man$\beta(1\rightarrow4)$GlcNAc$_2$ moiety. Clear electron density is observed between the $\beta(1\rightarrow4)$-linked Man residue and Asp-216 in Fbs1. Furthermore, Asp-216 is conserved in other F-box proteins that contain an F-box-associated domain, suggesting that it plays a role in the recognition of oligosaccharides. Man(IV) forms hydrogen bonds with the sidechain N^δ atom of Asn-159 through the O2 atom and with the sidechain N^η atom of Arg-214 through the O5 atom. On the other hand, Man(V) protrudes from the binding site and does not interact with Fbs1. These results indicate that the GlcNAc$_2$ core, $\beta(1\rightarrow4)$-linked Man(III), and $\alpha(1\rightarrow3)$-linked Man(IV) play significant roles in the binding to Fbs1. Whereas Man$_8$GlcNAc$_2$ is thought to be the major N-glycan among unfolded glycoproteins that are translocated into the cytosol for endoplasmic reticulum-associated degradation, our results indicate that Man$_3$GlcNAc$_2$ can be sufficiently recognized by the SCF^{Fbs1} complex. Indeed, various synthetic oligosaccharides were used to show that Man$_3$GlcNAc$_2$ and Man$_8$GlcNAc$_2$ have similar affinities for Fbs1 (22). On the other hand, the binding affinities of Man$_8$GlcNAc$_1$ and chitobiose for Fbs1 are several orders of magnitude lower than those of Man$_3$GlcNAc$_2$ and Man$_8$GlcNAc$_2$, indicating that Man$_3$GlcNAc$_2$ is required for efficient binding to Fbs1 (15, 22). Moreover, the binding site provides substrate selectivity and specificity based on its shape and hydrogen-bonding network.

There are limited contacts between the SBD and RNaseB; the interface involves only 514 Å^2 of surface-accessible area. The surface areas occupied by Man$_3$GlcNAc$_2$ and the protein portion of the substrate are 349 and 165 Å^2, respectively. In addition to the smaller contact area, the protein portion of RNaseB does not form a hydrogen bond with Fbs1, suggesting that Man$_3$GlcNAc$_2$, but not the protein in RNaseB, defines the interaction with Fbs1.

Linker Flexibility Might Accommodate a Range of Substrates. Two crystal forms were identified for Skp1–Fbs1 ($P3_221$ and $P2_12_12_1$) define form 1 and form 2, respectively). These two forms have essentially the same overall structure (rms deviation of 1.1 Å for the C^α atoms) (Fig. 4A). Whereas the Skp1 proteins are well aligned with each other, the SBD of Fbs1 in form 2 is tilted farther away from Skp1 by ≈3°. The 3° tilt angle of the SBD creates a 3-Å gap at the substrate-binding site and a 6-Å shift at the E2 active site. This flexibility seems to be due in part to the

linker-domain structure of Fbs1 (Fig. 4A). Residues 100–103 and 113–115 are shifted significantly compared with form 1. Although the linkage between the F-box and WD40 domains does not seem to be exceedingly rigid in the yeast Cdc4 structure, deletion of helix $\alpha5$ or the lengthening of helix $\alpha6$ due to an insertion of amino acid residues disrupts Cdc4 function in vivo, suggesting that the orientation and rigidity of the linkage between the F-box and the substrate-binding domains is important for SCF function (8). In the structure of Fbs1, the interaction between $\alpha5$ and the linker loop through van der Waals contacts (His-113 of the linker loop to Gln-115, Phe-119, and Arg-123 of $\alpha5$) is not rigid, and residues 104–108 of the linker domain are not visible in the electron density map. This structure indicates that the linkage between the F-box domain and the SBD of Fbs1 is somewhat flexible. This feature might allow the protein to accommodate a range of substrates (Fig. 4B).

Discussion

In this study, we determined the crystal structures of two crystal forms of the Skp1–Fbs1 complex and the SBD–RNaseB complex at 2.4-, 3.5-, and 2.7-Å resolutions, respectively. The structure of the Skp1–Fbs1 complex illustrates a different class of F-box proteins within the SCF ubiquitin ligase model. A model of the SCF^{Fbs1}–RNaseB–E2 complex was generated simply by superposition of the Skp1 subunits from the Skp1–Fbs1 and Skp1–Cul1–Rbx1 structures (PDB ID code 1LDK), the RING-finger domains derived from Rbx1 and from the c-Cbl subunit of the c-Cbl-UbcH7 structure (PDB ID code 1FBV) (23), the E2 subunits from the c-Cbl-UbcH7 structure, and the SBD-RNaseB structure. In this SCF^{Fbs1}-RNaseB model, RNaseB points toward the E2-binding site on Rbx1 (Fig. 5). The distance between the E2 active-site cysteine and the substrate-binding site is ≈60 Å, which is similar to the value that was reported previously (7, 8, 10). Despite differences in the sizes of the substrates and the positions of ubiquitinated lysine residues, the distance between the E2 active-site cysteine and the substrate-binding site is conserved among the SCF complexes. The same mechanism that allows the E2 active-site cysteine to reach the ubiquitinated lysine residues of the substrates is used independently of the type of F-box protein.

In the case of RNaseB, the distances between the E2 active-site cysteine and the lysine residues in RNaseB are 58.6–88.4 Å in the model of the SCF^{Fbs1}–RNaseB–E2 complex, whereas the

lysine residues in RNaseB are between 5.3 and 36.9 Å away from Asn-34. RNaseB is smaller than the minimum distance required to reach E2. Actually, SCF[Fbs1] was not able to ubiquitinate RNaseB *in vitro*. This could be because RNaseB is too small, the lysine residues are at the wrong positions, or RNaseB is fixed because of contacts between Man₃GlcNAc₂ and Fbs1.

One of the most important properties for ubiquitination is the rigidity of the SCF–ubiquitin–ligase complex structure, because it serves to correctly position the target protein and E2. The two crystal structures of the Skp1–Fbs1 complex described in the present study, however, show differences in the orientation of the SBD. We propose that SCF[Fbs1] has the ability to nonspecifically ubiquitinate glycoproteins targeted to the endoplasmic reticulum-associated degradation pathway. The protein portion of a target glycoprotein bound to Fbs1 may rotate at the linkage site between the innermost GlcNAc moiety and the asparagine residue, and the acceptor lysine residue can be located at a variety of positions. In SCF[Fbs1], the relative motion of the linker domain between the F-box domain and the SBD might be necessary to accommodate the different positions of the acceptor lysine residues in the various endoplasmic reticulum-associated degradation substrates.

SCF[Fbs1] is a functionally unique molecule that recognizes the innermost Man₃GlcNAc₂ in N-glycans as a marker of denatured proteins. Our results provide a mechanistic basis for the recognition and ubiquitination of various glycoproteins by SCF[Fbs1].

Materials and Methods

Protein Expression and Purification. The Skp1–Fbs1 complex was coexpressed from the pET28b plasmid (Novagen, Madison, WI) in BL21 (DE3) cells. Full-length Skp1 was expressed as a 6× His-tagged protein, and full-length Fbs1 was expressed as an untagged protein. The complex was purified stepwise by Ni affinity, anion exchange, and gel-filtration chromatography. The Skp1–Fbs1 complex was then concentrated to ≈10 mg/ml by ultrafiltration in 25 mM Tris·HCl (pH 7.5) and 1 mM DTT.

For the SBD–RNaseB complex (with SBD residues 105–297 of Fbs1), the SBD and RNaseB (Sigma, St. Louis, MO) were combined in a 1:1 molar ratio and purified by gel-filtration chromatography. Fractions containing the SBD–RNaseB complex were then concentrated to ≈10 mg/ml and used for crystallization.

Crystallization and Data Collection. Crystals of Skp1–Fbs1 and SBD–RNaseB were obtained at 20°C by using the sitting-drop vapor diffusion method. Skp1–Fbs1 crystals were grown from 2.0 M ammonium sulfate, 0.1 M sodium citrate (pH 5.7), and 30 mM chitobiose, which produced two crystal forms. The SBD–RNaseB crystals were prepared by using 2.0% (vol/vol) PEG 400, 0.1 M Hepes (pH 7.5), and 2.1 M ammonium sulfate.

Diffraction data sets for Skp1–Fbs1 and SBD–RNaseB were collected at beamline BL44XU (SPring-8, Hyogo, Japan). Data processing and reduction were carried out with the HKL program suite (24). The two crystal forms of Skp1–Fbs1 and the SBD–RNaseB crystals belong to the $P3_221$ (Skp1–Fbs1 form 1), $P2_12_12_1$ (Skp1–Fbs1 form 2), and $P432$ (SBD–RNaseB) space groups. Heavy-atom soaks of the Skp1–Fbs1 crystals (form 1) were performed in crystallization buffer with 1 mM thimerosal for 5 min. Data collection, phasing, and refinement statistics are summarized in Table 1.

Structure Determination and Refinement. The structure of Skp1–Fbs1 was determined by a combination of molecular replacement, single isomorphous replacement, and anomalous scattering with an Hg derivative. The initial single isomorphous replacement and anomalous scattering phases were calculated with SHARP (25) and then improved by density modification with DM (26). Molecular replacement with the program MOLREP (27) was used to locate the Skp1 and SBD portions of the complex with search models consisting of Skp1 from SCF (PDB ID code 1LDK) and the SBD of Fbs1 (PDB ID code 1UMH). The model was further built with the program COOT (28) and then was improved by several cycles of manual rebuilding and refinement with the program REFMAC5 (29). The structure of crystal form 2 was solved by molecular replacement using MOLREP with the refined model of form 1.

The structure of SBD–RNaseB was determined by using the molecular replacement technique, MOLREP, and the structures of the SBD and RNaseB. The refined model contains residues 123–297 of the SBD and residues 1–124 of RNaseB. Phasing and refinement statistics are summarized in Table 1. There are no residues in disallowed regions of the Ramachandran plot. Structure figures were generated by using MOLSCRIPT (30), RASTER3D (31), and CCP4MG (32).

1. Hershko A, Ciechanover A, Varshavsky A (2000) *Nat Med* 6:1073–1081.
2. Sherman MY, Goldberg AL (2001) *Neuron* 29:15–32.
3. Pickart CM (2001) *Annu Rev Biochem* 70:503–533.
4. Deshaies RJ (1999) *Annu Rev Cell Dev Biol* 15:435–467.
5. Jin J, Cardozo T, Lovering RC, Elledge SJ, Pagano M, Harper JW (2004) *Genes Dev* 18:2573–2580.
6. Yoshida Y (2003) *J Biochem (Tokyo)* 134:183–190.
7. Wu G, Xu G, Schulman BA, Jeffrey PD, Harper JW, Pavletich NP (2003) *Mol Cell* 11:1445–1456.
8. Orlicky S, Tang X, Willems A, Tyers M, Sicheri F (2003) *Cell* 112:243–256.
9. Schulman BA, Carrano AC, Jeffrey PD, Bowen Z, Kinnucan ER, Finnin MS, Elledge SJ, Harper JW, Pagano M, Pavletich NP (2000) *Nature* 408:381–386.
10. Zheng N, Schulman BA, Song L, Miller JJ, Jeffrey PD, Wang P, Chu C, Koepp DM, Elledge SJ, Pagano M, *et al.* (2002) *Nature* 416:703–709.
11. Hao B, Zheng N, Schulman BA, Wu G, Miller JJ, Pagano M, Pavletich NP (2005) *Mol Cell* 20:9–19.
12. Ellgaard L, Helenius A (2003) *Nat Rev Mol Cell Biol* 4:181–191.
13. Erhardt JA, Hynicka W, DiBenedetto A, Shen N, Stone N, Paulson H, Pittman RN (1998) *J Biol Chem* 273:35222–35227.
14. Yoshida Y, Chiba T, Tokunaga F, Kawasaki H, Iwai K, Suzuki T, Ito Y, Matsuoka K, Yoshida M, Tanaka K, *et al.* (2002) *Nature* 418:438–442.
15. Yoshida Y, Tokunaga F, Chiba T, Iwai K, Tanaka K, Tai T (2003) *J Biol Chem* 278:43877–43884.
16. Yoshida Y, Adachi E, Fukiya K, Iwai K, Tanaka K (2005) *EMBO Rep* 6:239–244.
17. Mizushima T, Hirao T, Yoshida Y, Lee SJ, Chiba T, Iwai K, Yamaguchi Y, Kato K, Tsukihara T, Tanaka K (2004) *Nat Struct Mol Biol* 11:365–370.
18. Aravind L, Koonin EV (1999) *J Mol Biol* 285:1353–1361.
19. Liang CJ, Yamashita K, Kobata A (1980) *J Biochem (Tokyo)* 88:51–58.
20. Williams RL, Greene SM, McPherson A (1987) *J Biol Chem* 262:16020–16031.
21. Ko TP, Williams R, McPherson A (1996) *Acta Crystallogr D* 52:160–164.
22. Hagihara S, Totani K, Matsuo I, Ito Y (2005) *J Med Chem* 48:3126–3129.
23. Zheng N, Wang P, Jeffrey PD, Pavletich NP (2000) *Cell* 102:533–539.
24. Otwinowski Z, Minor W (1997) *Methods Enzymol* 276:307–326.
25. Bricogne G, Vonrhein C, Flensburg C, Schiltz M, Paciorek W (2003) *Acta Crystallogr D* 59:2023–2030.
26. Collaborative Computational Project 4 (1994) *Acta Crystallogr D* 50:760–763.
27. Vagin AA, Teplyakov A (1997) *J Appl Crystallogr* 30:1022–1025.
28. Emsley P, Cowtan K (2004) *Acta Crystallogr D* 60:2126–2132.
29. Murshudov GN, Vagin AA, Dodson EJ (1997) *Acta Crystallogr D* 53:240–255.
30. Kraulis PJ (1991) *J Appl Crystallogr* 24:946–950.
31. Merritt EA, Murphy ME (1994) *Acta Crystallogr D* 50:869–873.
32. Potterton E, McNicholas S, Krissinel E, Cowtan K, Noble M (2002) *Acta Crystallogr D* 58:1955–1957.

Essential role for autophagy protein Atg7 in the maintenance of axonal homeostasis and the prevention of axonal degeneration

Masaaki Komatsu*[†‡], Qing Jun Wang[§¶], Gay R. Holstein[¶], Victor L. Friedrich, Jr.[¶], Jun-ichi Iwata*[†], Eiki Kominami[†], Brian T. Chait[§], Keiji Tanaka*, and Zhenyu Yue[¶‖]

[¶]Departments of Neurology and Neuroscience, Mount Sinai School of Medicine, New York, NY 10029; *Laboratory of Frontier Science, Tokyo Metropolitan Institute of Medical Science, Bunkyo-ku, Tokyo 113-8613, Japan; [†]Department of Biochemistry, Juntendo University School of Medicine, Bunkyo-ku, Tokyo 113-8421, Japan; [‡]Precursory Research for Embryonic Science and Technology, Japan Science and Technology Corporation, Kawaguchi 332-0012, Japan; and [§]Laboratory of Mass Spectrometry and Gaseous Ion Chemistry, Rockefeller University, New York, NY 10065

Autophagy is a regulated lysosomal degradation process that involves autophagosome formation and transport. Although recent evidence indicates that basal levels of autophagy protect against neurodegeneration, the exact mechanism whereby this occurs is not known. By using conditional knockout mutant mice, we report that neuronal autophagy is particularly important for the maintenance of local homeostasis of axon terminals and protection against axonal degeneration. We show that specific ablation of an essential autophagy gene, *Atg7*, in Purkinje cells initially causes cell-autonomous, progressive dystrophy (manifested by axonal swellings) and degeneration of the axon terminals. Consistent with suppression of autophagy, no autophagosomes are observed in these dystrophic swellings, which is in contrast to accumulation of autophagosomes in the axonal dystrophic swellings under pathological conditions. Axonal dystrophy of mutant Purkinje cells proceeds with little sign of dendritic or spine atrophy, indicating that axon terminals are much more vulnerable to autophagy impairment than dendrites. This early pathological event in the axons is followed by cell-autonomous Purkinje cell death and mouse behavioral deficits. Furthermore, ultrastructural analyses of mutant Purkinje cells reveal an accumulation of aberrant membrane structures in the axonal dystrophic swellings. Finally, we observe double-membrane vacuole-like structures in wild-type Purkinje cell axons, whereas these structures are abolished in mutant Purkinje cell axons. Thus, we conclude that the autophagy protein Atg7 is required for membrane trafficking and turnover in the axons. Our study implicates impairment of axonal autophagy as a possible mechanism for axonopathy associated with neurodegeneration.

axon | axonopathy | neurodegeneration | autophagosome | Purkinje cell

Macroautophagy is characterized by dynamic membrane rearrangements, involving the formation, trafficking, and degradation of double-membrane autophagic vacuoles (autophagosomes) in the cytoplasm. Macroautophagy (hereafter referred to as autophagy) is a highly regulated process, which can be induced by nutrient starvation, trophic factors, and stress (1). Despite recent advances in characterizing autophagy in several model systems, autophagic processes in the nervous system remain poorly understood. On one hand, nutrient deprivation has not been observed to induce autophagy in the mammalian brain (2), thus suggesting a specific regulatory system for autophagy that is not typically activated by starvation. On the other hand, a variety of conditions that cause neuronal stress or degeneration can lead to the accumulation of autophagosomes in neurons, thus implicating autophagy in these neuropathogenic processes (3, 4).

The axon is a highly specialized neuronal compartment that performs many functions independently from the cell body. After axotomy or excitotoxicity, double-membrane vacuoles resembling autophagosomes were originally observed to accumulate in dilated axon terminals that result from the injury (5, 6), a local phenomenon that is not observed in undisturbed axons. Autophagosome-like vacuoles have also been shown to be present in the dysfunctional or degenerating axons associated with a range of chronic neurodegenerative conditions, including Alzheimer's (7, 8), Parkinson's (9), Huntington's (10), and Creutzfeldt–Jakob (11) diseases and their animal models (12–14). These observations suggest a link between locally altered autophagy and axonopathy, which is one of the underlying mechanisms in neurodegeneration (15).

Although the biological significance of these autophagosomes-like vacuoles in degenerating axons is unclear, recent studies have shown that genetic inactivation of autophagy in the mouse CNS causes neurodegeneration accompanied by axonal dystrophy and the formation of intracellular ubiquitin-associated inclusions (16, 17). These studies suggest a role for basal levels of autophagy in neuronal protection and in protein quality control. However, the connection between the inactivation of autophagy and the observed axonal dystrophy and neurodegeneration remains to be determined. In addition, because autophagy was suppressed in all cell types in the CNS (including neurons and nonneuronal cells) (16, 17), it is not known whether the observed axonal dystrophy and neurodegeneration is cell-autonomous.

Here, we seek to further elucidate the physiological function of neuronal autophagy by generating conditional knockout mice with Purkinje cell-specific deletion of *Atg7*, an autophagy gene encoding E1-like enzyme in the two ubiquitin-like conjugation systems that are essential for the autophagosome biogenesis (18). We show that ablation of Atg7 leads to abnormal swellings and dystrophy of Purkinje cell axon terminals in the deep cerebellar nuclei (DCN). Subsequently, these *Atg7*-deletion mice develop cell-autonomous neurodegeneration of Purkinje cells, dendritic atrophy, and behavioral deficits. Moreover, double-membrane vacuole-like structures are formed in the distal ends of wild-type Purkinje cell axons, whereas they are absent in *Atg7*-deletion Purkinje cell axons.
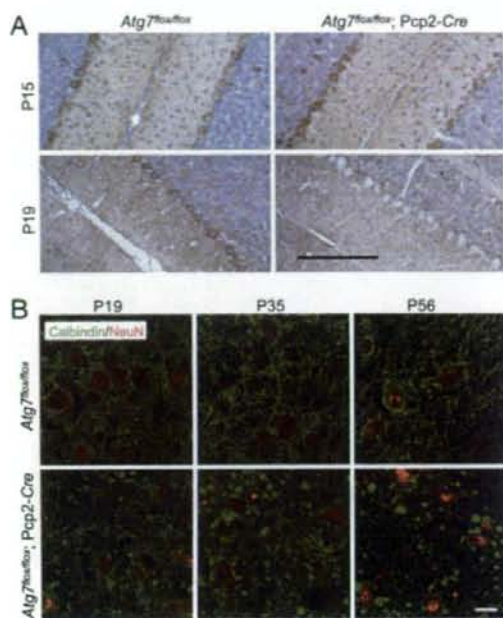
Fig. 1. Deletion of *Atg7* specifically in Purkinje cells caused progressive dystrophic swelling of axon terminals. (*A*) Immunohistochemistry of Atg7 protein expression in Purkinje cells of *Atg7^flox/flox* and *Atg7^flox/flox*;Pcp2-Cre mice at P15 and P19. The endogenous Atg7 protein was present at P15 but absent at P19 in the *Atg7^flox/flox*;Pcp2-Cre Purkinje cells. (Scale bar: 100 μm.) (*B*) Progression of the abnormal Purkinje cell axon terminal swellings in the DCN of *Atg7^flox/flox*;Pcp2-Cre mice (anti-calbindin immunofluorescent staining in green with anti-NeuN counterstained in red) at P19, P35, and P56. *Atg7^flox/flox* was used as control. (Scale bar: 20 μm.) *n* = 3–5.

Instead, the mutant Purkinje cell axon terminal swellings accumulate aberrant membranous structures. Our results suggest that autophagy is required for normal axon terminal membrane trafficking and turnover, and indicate an essential role of local autophagy in the maintenance of axonal homeostasis and prevention of axonal degeneration.

Results

Specific Depletion of Atg7 in Purkinje Cells Caused Cell-Autonomous Dystrophy and Degeneration of Axon Terminals. To generate Purkinje cell-specific deletion of *Atg7* in mice, we crossed mice harboring the floxed *Atg7* alleles (19) with transgenic mice expressing *Cre* recombinase under control of the Pcp2 (L7) promoter (20) to establish the mouse line *Atg7^flox/flox*;Pcp2-Cre. To determine when loss of the endogenous Atg7 protein occurred, we examined Atg7 expression in *Atg7^flox/flox*;Pcp2-Cre mice at postnatal day 15 (P15) and P19. At P15, Atg7 was expressed at similar levels in Purkinje cells of both mutant *Atg7^flox/flox*;Pcp2-Cre and the control *Atg7^flox/flox* mice, whereas at P19, despite residual expression in a small number of Purkinje cells (<12%), Atg7 immunostaining was largely diminished in *Atg7^flox/flox*;Pcp2-Cre Purkinje cells (>88%), but unchanged in the *Atg7^flox/flox* Purkinje cells (Fig. 1*A*). At P35, >95% Purkinje cells in *Atg7^flox/flox*;Pcp2-Cre showed no detectable Atg7 expression (data not shown). In addition, Atg7 deficiency in *Atg7^flox/flox*;Pcp2-Cre mice was specific for Purkinje cells because Atg7 is clearly present in the other cell types (Fig. 1*A*). Thus, the specific loss of Atg7 in Purkinje cells occurred largely between P15 and P19 in *Atg7^flox/flox*;Pcp2-Cre mice.

Next, we examined Purkinje cell axons in the DCN of

Atg7^flox/flox;Pcp2-Cre mice by immunofluorescent staining using an antibody against calbindin, a Purkinje cell marker. At P15, no morphological alteration was observed in the axons of *Atg7^flox/flox*;Pcp2-Cre Purkinje cells compared with those of *Atg7^flox/flox* Purkinje cells [supporting information (SI) Fig. 7], consistent with the presence of normal levels of Atg7 in *Atg7^flox/flox*;Pcp2-Cre Purkinje cells at this stage (Fig. 1*A*). However, at P19, *Atg7^flox/flox*;Pcp2-Cre Purkinje cell axons were abnormally dilated, as visualized by green fluorescence-labeled "endbulbs" (Fig. 1*B*). In addition, these Purkinje cell axonal swellings were labeled with the antibody raised against synaptophysin, the presynaptic terminal marker (SI Fig. 8), suggesting that they were terminals of Purkinje cell axons. The number and size of the swollen axon terminals in the DCN of the *Atg7^flox/flox*;Pcp2-Cre were markedly increased at P35 in comparison with those at P19 (Fig. 1*B*). At P56, the number of such axonal dystrophic swellings of the mutant Purkinje cells was noticeably decreased in comparison with that at P35, suggesting that many of these swollen axons had degenerated by this age (Fig. 1*B*). These data demonstrated that deletion of *Atg7* caused cell-autonomous axonal dystrophy and degeneration in Purkinje cells.

Axonal Dystrophic Swellings of *Atg7^flox/flox*;Pcp2-Cre Purkinje Cells Were Devoid of GFP-Light Chain 3 (LC3)-Labeled Puncta and Exhibited Increased Levels of p62/SQSTM1. Transgenic mice producing GFP fused with microtubule-associated protein 1 light chain 3 (LC3), a specific marker for autophagosomes (21), were previously generated to monitor autophagosomes *in vivo* (2). By expressing GFP-LC3 in *Lurcher* mice (GFP-LC3/*Lurcher*), we showed that a large number of autophagosomes were formed in the dystrophic axon terminals of *Lurcher* Purkinje cells (Fig. 2*Ad*), providing *in vivo* evidence for the induction of autophagy in response to *Lurcher*-induced excitotoxicity (22). To assess autophagic activity in the dystrophic axons of *Atg7^flox/flox*;Pcp2-Cre Purkinje cells, we crossed transgenic GFP-LC3 with *Atg7^flox/flox*;Pcp2-Cre mice (*Atg7^flox/flox*;Pcp2-Cre/GFP-LC3). Despite intense GFP-LC3 accumulation in the axonal dystrophic swellings of Purkinje cells in *Atg7^flox/flox*;Pcp2-Cre/GFP-LC3 mice at P35, no GFP-LC3 fluorescent puncta characteristic of autophagosomes were observed in these swellings (Fig. 2*A b* and *c*). We contrasted this finding to our observation of GFP-LC3 puncta in Purkinje cell axons GFP-LC3/*Lurcher* mice (Fig. 2*Ad*) (22). In addition, no GFP-LC3 puncta were observed in the somata or dendrites of *Atg7^flox/flox*;Pcp2-Cre/GFP-LC3 Purkinje cells (Fig. 2*A f* and *g*), again in contrast to the observation of GFP-LC3 puncta in the somata and dendrites of GFP-LC3/*Lurcher* Purkinje cells (Fig. 2*Ah*) (22).

It has been shown that inhibition of autophagy is correlated with increased levels of the polyubiquitin binding protein p62/SQSTM1 (22, 23). We thus examined the levels of p62/SQSTM1 in *Atg7^flox/flox*;Pcp2-Cre Purkinje cells. As detected with anti-p62/SQSTM1 immunofluorescent staining, p62/SQSTM1 was markedly accumulated in the axonal dystrophic swellings (Fig. 2*B*, arrows) and somata (SI Fig. 9) of *Atg7^flox/flox*;Pcp2-Cre Purkinje cells in comparison with *Atg7^flox/flox* Purkinje cells. It is also noteworthy that the dystrophic axonal swellings in *Lurcher* Purkinje cells did not have detectable p62/SQSTM1 immunofluorescent staining (SI Fig. 10). These results provided molecular evidence for impaired autophagic activity in the dystrophic axons of *Atg7^flox/flox*;Pcp2-Cre Purkinje cells, but not in the dystrophic axons of *Lurcher* Purkinje cells.

Atg7^flox/flox;Pcp2-Cre Purkinje Cells Exhibited Normal Dendritic Tree and Spine Morphology at P56. Despite the remarkable dystrophy and degeneration of Purkinje cell axon terminals in the DCN of *Atg7^flox/flox*;Pcp2-Cre mice at P35 and P56, the cerebellar cortex displayed little change in its overall size and organization (Fig. 3*A*). For example, at P35 and P56, *Atg7^flox/flox*;Pcp2-Cre mice and
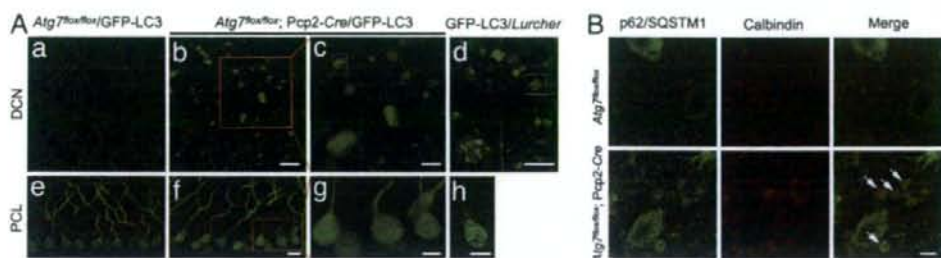
Fig. 2. The axonal dystrophic swellings of the *Atg7*-deficient Purkinje cells contained no GFP-LC3 labeled autophagosomes but accumulated p62/SQSTM1. (*A*) The absence of GFP-LC3 puncta in Purkinje cell axonal dystrophic swellings (*b* and *c*) and somata (*f* and *g*) of *Atg7^flox/flox*;Pcp2-Cre/GFP-LC3 mice (P35). GFP-LC3 puncta were found in GFP-LC3/*Lurcher* Purkinje cell axonal dystrophic swellings (*d*) and somata (*h*) (P12). DCN (*a*) and Purkinje cell layer (PCL) (*e*) of control mice Atg7^flox/flox/GFP-LC3 are shown. (Scale bars: *a*, *b*, *e*, and *f*, 20 μm; *c*, *d*, *g*, and *h*, 10 μm.) (*B*) Anti-p62/SQSTM1 immunofluorescent staining (in green) showed accumulation of p62/SQSTM1 in Purkinje cell axonal dystrophic swellings (calbindin labeling in red) (white arrows) in the DCN of *Atg7^flox/flox*;Pcp2-Cre mice at P56. *Atg7^flox/flox* was used as control. (Scale bar: 10 μm.)

Atg7^flox/flox mice did not exhibit significant difference in their cerebellar molecular layer thickness (Fig. 3 *A* and *B*). To evaluate changes in dendritic tree and spine morphology, we examined the expression pattern of metabotropic glutamate receptor 1α (mGluR1α) protein, a marker for parallel fiber–Purkinje cell synapses. No difference in localization and intensity of the anti-mGluR1α immunofluorescent staining was observed between the *Atg7^flox/flox*;Pcp2-Cre and *Atg7^flox/flox* cerebellar molecular layers at either P35 (data not shown) or P56 (Fig. 3*C*). Thus, *Atg7* deletion had little effect on Purkinje cell dendritic tree and spine morphology up to at least P56. We conclude that *Atg7*
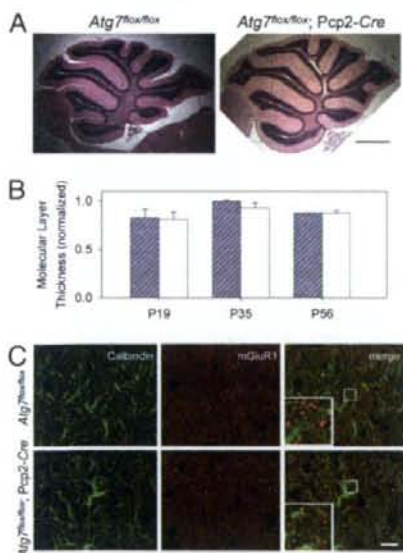

Fig. 3. Deletion of *Atg7* in Purkinje cells had little effect on the morphology of cerebellar cortex, Purkinje cell dendritic tree and spines in *Atg7^flox/flox*;Pcp2-Cre mice at P56. (*A*) H&E-stained images of midsagittal sections from *Atg7^flox/flox* and *Atg7^flox/flox*;Pcp2-Cre cerebella at P56. (Scale bar: 0.5 mm.) n = 3–5. (*B*) Quantification of the molecular layer thickness (as the distance between lobules V and VI of the Purkinje cell layer divided by 2) from the cerebellar midsagittal sections of *Atg7^flox/flox* and *Atg7^flox/flox*;Pcp2-Cre mice at P19, P35, and P56. n = 3–5. (*C*) Immunofluorescent staining of cerebellar midsagittal sections shows normal localization and appearance of mGluR1α (in red) in *Atg7^flox/flox*;Pcp2-Cre mice compared with *Atg7^flox/flox* mice at P56. Green indicates anti-calbindin. (Scale bar: 10 μm.) n = 3.

deletion in Purkinje cells elicit differential effects on the dendritic and axonal compartments, suggesting that the axon terminals are particularly vulnerable to autophagy deficiency.

Axonal Dystrophy Preceded Cell-Autonomous Degeneration of Purkinje Cells and Behavioral Deficits in *Atg7^flox/flox*;Pcp2-Cre Mice. To further evaluate the effects of *Atg7* deletion, we assayed for Purkinje cell degeneration and mouse behavioral deficits. Whereas the Purkinje cell axonal dystrophic swellings in the DCN of *Atg7^flox/flox*;Pcp2-Cre mice first became apparent at P19 and grew severe at P35 (Fig. 2*A*), no significant difference in Purkinje cell numbers was observed between the *Atg7^flox/flox*;Pcp2-Cre and *Atg7^flox/flox* mice at both ages (Fig. 4 *A* and *B*). However, at P56, the number of Purkinje cells in *Atg7^flox/flox*;Pcp2-Cre mice was reduced by 28.4% (P < 0.0005) compared with *Atg7^flox/flox* mice (Fig. 4 *A* and *B*). Thus, loss of Purkinje cells in *Atg7^flox/flox*;Pcp2-Cre mice occurred between P35 and P56. In comparison, the onset of axonal dystrophy began as early as P19. In addition, levels of GluRδ2 (a Purkinje cell-specific glutamate receptor subtype) in *Atg7^flox/flox*;Pcp2-Cre cerebellar extract were not reduced until P56 (SI Fig. 11), further supporting that the onset of axon dystrophy was earlier than Purkinje cell degeneration in *Atg7^flox/flox*;Pcp2-Cre mice.

Next, we assessed the locomotive behaviors in *Atg7^flox/flox*;Pcp2-Cre mice by limb-clasping, rotarod, and gait analyses at different postnatal ages. At P19 and P35, *Atg7^flox/flox*;Pcp2-Cre mice appeared normal and did not show any difference in performance compared with their control *Atg7^flox/flox* littermates (data not shown). At P56, *Atg7^flox/flox*;Pcp2-Cre and *Atg7^flox/flox* mice performed equally well on the rotarod and gait analyses (Fig. 4 *C* and *D*). However, 5 of 13 *Atg7^flox/flox*;Pcp2-Cre mice (38.5%) displayed limb-clasping reflexes on tail suspension, in comparison with 0 of 10 of their control littermates (P < 0.01). Thus, at P56, despite the 28.4% loss of Purkinje cells (Fig. 4*B*), *Atg7^flox/flox*;Pcp2-Cre mice displayed only mild behavioral impairment. In contrast, at 1 year, these mice demonstrated severe behavioral disorders in locomotion and motor coordination when evaluated in all three behavioral tests (Fig. 4 *C* and *D*; data not shown).

We summarize the temporal relationship of the morphological alterations, differential pathology in different compartments of Purkinje cells, and behavioral changes in *Atg7^flox/flox*;Pcp2-Cre mice in SI Table 1. These results demonstrate that axonal dystrophic swelling is an early pathogenic event and is likely to be a direct result of impairment of local autophagy in axon terminals.

Aberrant Membrane Structures Accumulated in the Dystrophic Axon Terminals of *Atg7^flox/flox*;Pcp2-Cre Purkinje Cells. To further assess the effect of impairment of autophagy on axon terminals, we characterized the axonal dystrophic swellings of *Atg7^flox/flox*;Pcp2-
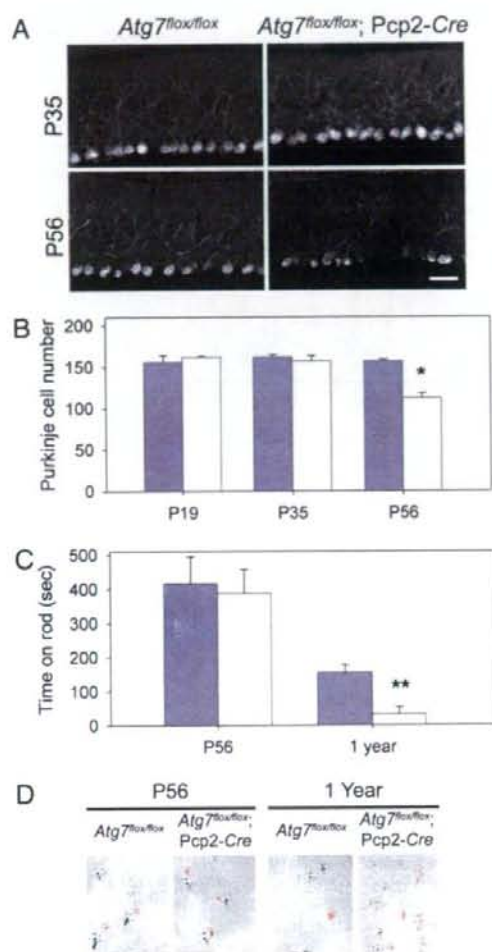
Fig. 4. Time course of Purkinje cell degeneration and locomotive behavioral deficits in *Atg7$^{flox/flox}$*;Pcp2-Cre mice. (*A*) Anti-calbindin immunofluorescent staining of the cerebellar midsagittal sections of *Atg7$^{flox/flox}$* and *Atg7$^{flox/flox}$*;Pcp2-Cre mice at P35 and P56. (*B*) Quantitation of Purkinje cells at lobules IV–V of the midsagittal sections of *Atg7$^{flox/flox}$* and *Atg7$^{flox/flox}$*;Pcp2-Cre mice at P19, P35, and P56 based on H&E-stained images. n = 3, 3, and 3 for *Atg7$^{flox/flox}$* at P19, P35, and P56, respectively. n = 2, 3, and 5 for *Atg7$^{flox/flox}$*;Pcp2-Cre at P19, P35, and P56, respectively (∗, $P < 0.0005$). (*C*) At P56, *Atg7$^{flox/flox}$* and *Atg7$^{flox/flox}$*;Pcp2-Cre mice showed no significant difference in the time spent on the rod in rotarod assay. At 1 year, *Atg7$^{flox/flox}$* mice spent much longer time on the rod than *Atg7$^{flox/flox}$*;Pcp2-Cre mice (∗∗, $P < 0.05$). (*D*) In gait analyses at P56, *Atg7$^{flox/flox}$* and *Atg7$^{flox/flox}$*;Pcp2-Cre mice showed similar step width and overlapping of forefeet and hindfeet (forefeet, red; hindfeet, black). At 1 year old, *Atg7$^{flox/flox}$*;Pcp2-Cre mice showed shorter step width than *Atg7$^{flox/flox}$* mice as well as nonoverlapping forefeet and hindfeet (left feet, black; right feet, red). For both *C* and *D*, n = 5 at P56; n = 3 and 4 at 1 year.

Cre Purkinje cells by transmission electron microscopy. The cross-sections of the Purkinje cell axon terminals in the DCN of the *Atg7$^{flox/flox}$* mice were normally 0.5–2 μm in diameter (Fig. 5*A*, white arrows). Remarkably, the swollen Purkinje cell axon terminals in the DCN of the *Atg7$^{flox/flox}$*;Pcp2-Cre mice often spanned 1–6 μm in diameter (Fig. 5 *B–F*, black arrows) and differed profoundly in their morphology from the axonal dystrophic swellings observed in *Lurcher* Purkinje cells (Fig. 5*G*,

black arrows). The Purkinje cell axonal dystrophic swellings of *Lurcher* mice contained a large number of autophagosomes/autolysosomes (Fig. 5*G*), whereas those of the *Atg7$^{flox/flox}$*;Pcp2-Cre mice were devoid of autophagosomes (Fig. 2 and 6*Af*). However, these autophagosome-free swellings of the *Atg7$^{flox/flox}$*;Pcp2-Cre Purkinje cell axons often contained abnormal organelles or membrane structures (Fig. 5 *B–F*, white arrows), including stacks of cisternal membranes that formed lamellar bodies (Fig. 5 *B* and *E*, white arrows) (24), large and elaborate cisternal arrays and filaments (Fig. 5*F*, white arrow), and highly convoluted double-membrane whorls that occupied 1.5–2 μm of the swollen terminal (Fig. 5 *C* and *D*, white arrows). The exact nature of these aberrant structures was not clear; they were rarely seen in the somata of *Atg7$^{flox/flox}$*;Pcp2-Cre Purkinje cells (data not shown) or in the *Atg7$^{flox/flox}$* Purkinje cells axons (Fig. 5*A*). However, it is noteworthy that the formation of convoluted membrane whorls was previously described in hepatocytes with *Atg7* deletion and was attributed to a failure in autophagic degradation (19). Our observations suggest a conserved function for autophagy in the clearance of cellular membranes and/or lipids in both axon terminals and hepatocytes.

Vacuole-Like Structures with Double Membranes Were Formed in Normal Purkinje Cell Axons but Were Absent in the Dystrophic Axon Terminals of *Atg7$^{flox/flox}$*;Pcp2-Cre Purkinje Cells. Interestingly, through further ultrastructural analysis, we observed vacuole-like structures with double membranes in the myelinated Purkinje cell axons in the DCN of control *Atg7$^{flox/flox}$* mice (Fig. 6*Aa* and SI Fig. 12). These structures typically appeared to be closed and had diameters of 0.1–0.5 μm (Fig. 6*Aa*). We occasionally observed these double-membrane vacuole-like structures in the process of formation (Fig. 6*A b–e* and SI Fig. 12*A*). Many of these developing double-membrane vacuole-like structures appeared to be formed through invagination of the axolemma along the myelinated layers (Fig. 6*A b* and *c*, SI Fig. 12*A*), reminiscent of invasion by oligodendrocytic processes (25, 26). Some of them appear to be continuous with the axonal plasma membrane (Fig. 6*A d* and *e*), which are enwrapping portions of axoplasm (27). The average number of these distinct double-membrane vacuole-like structures (both closed and in the process of formation) in Purkinje cell axons of *Atg7$^{flox/flox}$* mice was ≈0.9/50 μm^2 (Fig. 6*B*). In contrast, these structures were virtually absent in the *Atg7$^{flox/flox}$*;Pcp2-Cre mice (Fig. 6 *Af*, *B*, and *C*). Although we have yet to determine the exact nature of the vacuole-like structures with double membranes and their relationship with autophagosomes, our results suggested that *Atg7* was required for the formation of these distinct structures in axon terminals of normal Purkinje cells.

Discussion

Axonal dystrophic swelling is a hallmark of CNS axonopathy, which can be triggered by neuronal injuries, excitotoxicity, and various neurodegenerative conditions. Despite the prevalence of this pathology, the molecular mechanisms underlying axonopathy as well as the connection between axonopathy and neurodegeneration remain poorly understood (28). A critical question is whether axonal dystrophy and degeneration precede neuronal cell death or are secondary to neurodegeneration. Here, we analyzed the time course of pathological events after the deletion of the autophagy gene *Atg7* in cerebellar Purkinje cells. We showed that axonal dystrophy and degeneration caused by ablation of *Atg7* occurred much earlier than the onset of neuronal death, indicating that axonal dystrophy was not secondary to neurodegeneration. In addition, axonal dystrophy and degeneration was a cell-autonomous event, which precluded the action of glia as the primary cause of the axonal dystrophy in *Atg7$^{flox/flox}$*;Pcp2-Cre mice. Although this study was limited to Purkinje cells for the purpose of cell type-specific study of autophagy, axonal dystrophies occurred widely in many
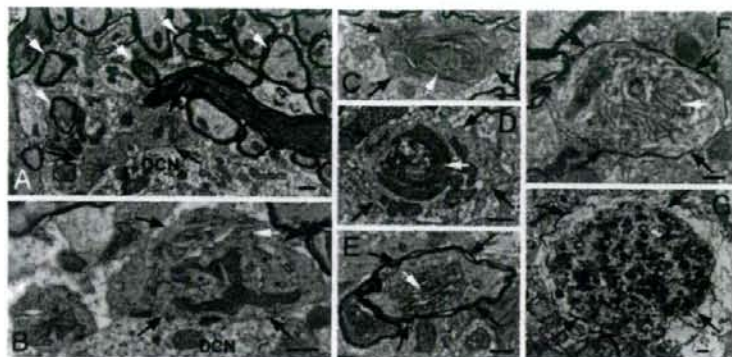
- 369 -

Fig. 5. Deletion of *Atg7* in Purkinje cells led to aberrant membrane structures in the axonal dystrophic swellings. Ultrastructural image of normal myelinated Purkinje cell axons (white arrows) and axon terminals (black arrows) in the DCN of *Atg7floxiflox* mice (*A*) and Purkinje cell axonal dystrophic swellings (black arrows) in the DCN of *Atg7floxiflox*;Pcp2-Cre mice (*B–F*). (*B* and *E*) Stacks of cisternal membranes (white arrows). (*C* and *D*) Convoluted double-membrane whorls (white arrows). (*F*) The arrays of abnormal filaments (white arrows). (*G*) A dystrophic axon (black arrows) of *Lurcher* Purkinje cells containing numerous autophagosomes. (Scale bars: 500 nm.)

regions of the mutant mouse brain with *Atg7* or *Atg5* deletion (16, 17). We speculate that the axonal dystrophy associated with various types of neurons in these mutant mice are also cell-autonomous events caused by the absence of neuronal autophagy. Importantly, our results implied that interference in local autophagy would have a deleterious effect on axons, a potential mechanism of axonopathies involving impaired autophagy. Furthermore, we showed that deletion of *Atg7* had little effect on the overall morphology of the Purkinje cell dendritic arbors at a stage when axon terminals displayed massive dystrophy and degeneration. These differential effects of *Atg7* deletion suggested that basal levels of autophagy played a particularly important role in housekeeping functions in axon terminals and in protection against axonal degeneration.

We showed that *Atg7* was indispensable for the formation of the distinctive vacuole-like structures with double membranes, which were normally present within wild-type Purkinje cell axons. These structures have not been described previously in the wild-type Purkinje cell axons. Although the majority of these structures were likely derived from invagination of neighboring oligodendrocytes (Fig. 6*A b* and *c* and SI Fig. 12*A*) (25, 26), some of them appeared

to originate from axonal subsurface cisternae (27) or smooth endoplasmic reticulum (29) (Fig. 6*A d* and *e*). Although we have yet to determine the nature of these structures, we cannot exclude the possibility that some of these structures are autophagosome-related vacuoles. A previous study has shown the presence and transport of autophagosomes in the axons of cultured sympathetic neurons, despite that the physiological function of autophagy in the axons is unknown (30). Regardless of the nature of these vacuole-like structures, *Atg7* deletion abolished their formation, and caused axonal swelling and accumulation of aberrant membrane structures in these swellings. These results established an important role of *Atg7* in regulating local membrane trafficking and turnover. However, an important question arising from these results is whether the requirement of *Atg7* for the formation of the double-membrane vacuole-like structures is somehow connected to autophagy or associated with a specific Atg7 function independent of autophagy. Current evidence suggests that *Atg7* function is exclusively associated with autophagy. Consistent with this idea, the abolishment of the double-membrane vacuole-like structures caused by *Atg7* deletion can be explained by the failure of autophagy, which would
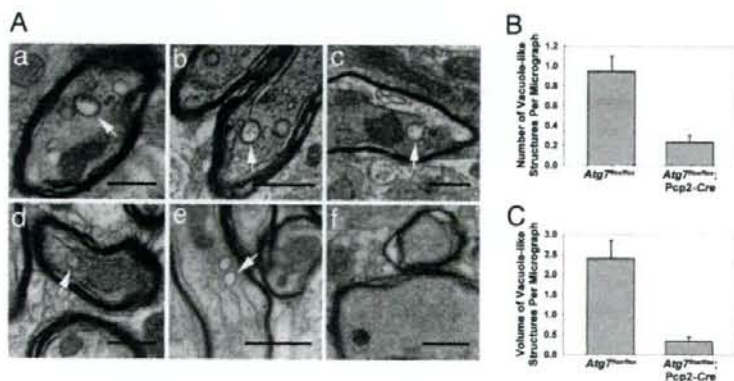

Fig. 6. Deletion of *Atg7* in Purkinje cells abolished double-membrane vacuole-like structures in their axon terminals in the DCN. (*A*) Ultrastructural images show the presence of vacuole-like structures with double membranes in Purkinje cell preterminal axons of *Atg7floxiflox* mice (*a–e*, white arrows) and the abolishment · of these structures in *Atg7floxiflox*;Pcp2-Cre mice (*f*) at P35. (Scale bars: 0.5 μm.) (*B*) Comparison of the numbers of these vacuole-like structures per transmission electron microscopy micrograph (50 μm²) in the DCN of *Atg7floxiflox*;Pcp2-Cre versus *Atg7floxiflox* mice (ratio, 4.0; $P = 0.00003$). (*C*) Comparison of the volume fraction of double-membrane vacuole-like structures by point counting of transmission electron microscopy micrographs in the DCN of *Atg7floxiflox*;Pcp2-Cre versus *Atg7floxiflox* mice (ratio, 6.9; $P = 0.00002$).

Komatsu *et al.*

normally participate in the formation of these structures. Thus, we hypothesize that, in addition to the role in protein quality control (16, 17), neuronal autophagy regulates membrane homeostasis in the axon terminals. Furthermore, we showed that deletion of *Atg7* caused the axonal terminal swelling, which was a reminiscence of hepatic cell swelling in *Atg7*-deleted mouse liver (19). It is conceivable that axon terminals and hepatocytes may share a similar mechanism for cell (or cellular compartment) size control, which requires autophagy (31).

Previous morphological studies have consistently shown the presence of large numbers of autophagosome-like vacuoles in axonal dystrophic swellings of injured neurons (4–13). We have previously demonstrated that induction of autophagy in *Lurcher* Purkinje cells involved accumulation of autophagosomes in the dystrophic axons (22). In contrast, our present study shows that the axonal swellings of Purkinje cells in *Atg7^floxiflox*;Pcp2-Cre mice were devoid of vacuoles that resembled the autophagosomes observed in *Lurcher* mice. Although our present study demonstrates a role for basal levels of autophagy in axonal protection and indicates that altered autophagy could serve as an adaptive response for remodeling the axon terminals for regeneration (3, 22), we cannot exclude the possibility that up-regulation of autophagy in dystrophic axons is actually destructive, causing overdegradation of axonal structures. This possibility can be tested, in principle, by genetic crossing of the autophagy-deficient mice with diseased mice containing the autophagosome-like vacuoles in dystrophic axons or cell bodies.

In summary, our study provides genetic and molecular evidence for the indispensable role of neuronal autophagy in the maintenance of axonal homeostasis, particularly in local membrane trafficking and turnover. Perturbation of local autophagy in the axons leads to axonopathy. We believe that it is important to study the connection between axonal autophagy impairment and human neuropathological conditions associated with axonal dystrophy.

Materials and Methods

Antibodies. Antibodies used were mouse monoclonal anti-calbindin D-28K (Swant, Bellinzona, Switzerland), anti-calbindin (Sigma, St. Louis, MO), anti-GluRδ2 (BD Transduction Laboratories, San Diego, CA), anti-p62 (American Research Products, Belmont, MA), Cy3-conjugated anti-mouse and anti-rabbit IgG (Upstate Biotechnology, Lake Placid, NY), and NeuN, mGluR1α, and actin antibodies (Chemicon International, Temecula, CA). Anti-Atg7 is described in ref. 19.

Animals. Pcp2-Cre transgenic mice (20) (The Jackson Laboratory, Bar Harbor, ME) and *Atg7^floxiflox* mice (19) were crossed to produce *Atg7^floxiflox*;Pcp2-Cre mice. *Atg7^floxiflox*;Pcp2-Cre mice and GFP-LC3 transgenic mice (2) were crossed to produce *Atg7^floxiflox*;Pcp2-Cre/GFP-LC3 mice.

Histological Examination. Mice were fixed by cardiac perfusion with 0.1 M phosphate buffer containing 4% paraformaldehyde. The color images of the Meyer's H&E-stained midsagittal cryosections (10 μm) of cerebella were acquired with a 20× objective lens and a color CCD camera, and later assembled to full images in Photoshop for the quantification of Purkinje cells. Immunofluorescent stained cerebellar samples were prepared as described in ref. 22 and examined by using confocal microscopy.

Behavioral Analyses. Motor function was assessed by the limb-clasping test, rotarod assay, and gait analysis (*SI Materials and Methods*).

Electron Microscopy. Tissue samples were obtained from three *Atg7^floxiflox* mice and three *Atg7^floxiflox*;Pcp2-Cre mice. Details of the experiment are described in *SI Materials and Methods*. In brief, thin sections (70 nm) of the lateral cerebellar nucleus and cerebellar cortex were prepared and examined by transmission electron microscopy (H7500; Hitachi, Tokyo, Japan). A double-blind point-counting method was used to quantify double-membrane vacuole-like structures in 55 micrographs of either *Atg7^floxiflox* or *Atg7^floxiflox*;Pcp2-Cre mice. The total number of these structures overlying at least one intersection of a Photoshop-generated grid was counted to be 52 and 13 for *Atg7^floxiflox* and *Atg7^floxiflox*;Pcp2-Cre samples, respectively. The total number of intersections within these structures was 132 and 19 for *Atg7^floxiflox* and *Atg7^floxiflox*;Pcp2-Cre samples, respectively.

Statistical Analyses. The equality of the variance was first tested by using the *F* test. Pair-wise comparisons were calculated by using one-tailed Student's *t* test. The standard error was calculated for each sample.

1. Levine B, Klionsky DJ (2004) *Dev Cell* 6:463–477.
2. Mizushima N, Yamamoto A, Matsui M, Yoshimori T, Ohsumi Y (2004) *Mol Biol Cell* 15:1101–1111.
3. Rubinszstein DC, DiFiglia M, Heintz N, Nixon RA, Qin ZH, Ravikumar B, Stefanis L, Tolkovsky A (2005) *Autophagy* 1:11–22.
4. Yue Z, Horton A, Bravin M, DeJager PL, Selimi F, Heintz N (2002) *Neuron* 35:921–933.
5. Dixon JS (1967) *Nature* 215:657–658.
6. Matthews MR, Raisman G (1972) *Proc R Soc Lond Ser B* 181:43–79.
7. Nixon RA, Wegiel J, Kumar A, Yu WH, Peterhoff C, Cataldo A, Cuervo AM (2005) *J Neuropathol Exp Neurol* 64:113–122.
8. Cataldo AM, Hamilton DJ, Barnett JL, Paskevich PA, Nixon RA (1996) *J Neurosci* 16:186–199.
9. Anglade P, Vyas S, Javoy-Agid F, Herrero MT, Michel PP, Marquez J, Mouatt-Prigent A, Ruberg M, Hirsch EC, Agid Y (1997) *Histol Histopathol* 12:25–31.
10. Roizin L, Stellar S, Willson N, Whittier J, Liu JC (1974) *Trans Am Neurol Assoc* 99:240–243.
11. Sikorska B, Liberski PP, Giraud P, Kopp N, Brown P (2004) *Int J Biochem Cell Biol* 36:2563–2573.
12. Yu WH, Cuervo AM, Kumar A, Peternoff CM, Schmidt SD, Lee JH, Mohan PS, Mercken M, Farmery MR, Tjernberg LO, et al. (2005) *J Cell Biol* 171:87–98.
13. Lin WL, Lewis J, Yen SH, Hutton M, Dickson DW (2003) *J Neurocytol* 32:1091–1105.
14. Li H, Li SH, Yu ZX, Shelbourne P, Li XJ (2001) *J Neurosci* 21:8473–8481.
15. Coleman MP, Perry VH (2002) *Trends Neurosci* 25:532–537.
16. Komatsu M, Waguri S, Chiba T, Murata S, Iwata J, Tanida I, Ueno T, Koike M, Uchiyama Y, Kominami E, et al. (2006) *Nature* 441:880–884.
17. Hara T, Nakamura K, Matsui M, Yamamoto A, Nakahara Y, Suzuki-Migishima R, Yokoyama M, Mishima K, Saito I, Okano H, et al. (2006) *Nature* 441:885–889.
18. Ohsumi Y, Mizushima N (2004) *Semin Cell Dev Biol* 15:231–236.
19. Komatsu M, Waguri S, Ueno T, Iwata J, Murata S, Tanida I, Ezaki J, Mizushima N, Ohsumi Y, Uchiyama Y, et al. (2005) *J Cell Biol* 169:425–434.
20. Barski JJ, Dethleffsen K, Meyer M (2000) *Genesis* 28:93–98.
21. Kabeya Y, Mizushima N, Ueno T, Yamamoto A, Kirisako T, Noda T, Kominami E, Ohsumi Y, Yoshimori T (2000) *EMBO J* 19:5720–5728.
22. Wang QJ, Ding Y, Kohtz S, Mizushima N, Cristea IM, Rout MP, Chait BT, Zhong Y, Heintz N, Yue Z (2006) *J Neurosci* 26:8057–8068.
23. Bjorkoy G, Lamark T, Brech A, Outzen H, Perander M, Overvatn A, Stenmark H, Johansen T (2005) *J Cell Biol* 171:603–614.
24. Banno T, Kohno K (1998) *J Comp Neurol* 402:252–263.
25. Zhang P, Land W, Lee S, Juliani J, Lefman J, Smith SR, Germain D, Kessel M, Leapman R, Rouault TA, et al. (2005) *J Struct Biol* 150:144–153.
26. Eddleman CS, Ballinger ML, Smyers ME, Fishman HM, Bittner GD (1998) *J Neurosci* 18:4029–4041.
27. Li YC, Li YN, Cheng CX, Sakamoto H, Kawate T, Shimada O, Atsumi S (2005) *Neurosci Res* 53:298–303.
28. Coleman M (2005) *Nat Rev Neurosci* 6:889–898.
29. Broadwell RD, Cataldo AM (1984) *J Comp Neurol* 230:231–248.
30. Hollenbeck PJ (1993) *J Cell Biol* 121:305–315.
31. Hosokawa N, Hara Y, Mizushima N (2006) *FEBS Lett* 580:2623–2629.

Homeostatic Levels of p62 Control Cytoplasmic Inclusion Body Formation in Autophagy-Deficient Mice

Masaaki Komatsu,[1,2,3] Satoshi Waguri,[4] Masato Koike,[5] Yu-shin Sou,[1,2] Takashi Ueno,[2] Taichi Hara,[6] Noboru Mizushima,[6,7] Jun-ichi Iwata,[1,2] Junji Ezaki,[2] Shigeo Murata,[1] Jun Hamazaki,[1] Yasumasa Nishito,[1] Shun-ichiro Iemura,[8] Tohru Natsume,[8] Toru Yanagawa,[9] Junya Uwayama,[9] Eiji Warabi,[9] Hiroshi Yoshida,[9] Tetsuro Ishii,[9] Akira Kobayashi,[10] Masayuki Yamamoto,[10] Zhenyu Yue,[11] Yasuo Uchiyama,[5] Eiki Kominami,[2] and Keiji Tanaka[1,*]

[1]Laboratory of Frontier Science, Tokyo Metropolitan Institute of Medical Science, Bunkyo-ku, Tokyo 113-8613, Japan
[2]Department of Biochemistry, Juntendo University School of Medicine, Bunkyo-ku, Tokyo 113-8421, Japan
[3]PRESTO, Japan Science and Technology Corporation, Kawaguchi 332-0012, Japan
[4]Department of Anatomy and Histology, Fukushima Medical University School of Medicine, Hikarigaoka, Fukushima 960-1295, Japan
[5]Department of Cell Biology and Neurosciences, Osaka University Graduate School of Medicine, Suita, Osaka 565-0871, Japan
[6]Department of Physiology and Cell Biology, Tokyo Medical and Dental University Graduate School and Faculty of Medicine, Bunkyo-ku, Tokyo 113-8519, Japan
[7]SORST, Japan Science and Technology Corporation, Kawaguchi 332-0012, Japan
[8]National Institutes of Advanced Industrial Science and Technology, Biological Information Research Center (JBIRC), Kohtoh-ku, Tokyo 135-0064, Japan
[9]Graduate School of Comprehensive Human Sciences, University of Tsukuba, Tennoudai, Tsukuba 305-8575, Japan
[10]Department of Medical Biochemistry and ERATO-JST, Tohoku University Graduate School of Medicine, Aoba-ku, Sendai 980-8575, Japan
[11]Departments of Neurology and Neuroscience, Mount Sinai School of Medicine, New York, NY 10029, USA
*Correspondence: tanakak@rinshoken.or.jp
DOI 10.1016/j.cell.2007.10.035

SUMMARY

Inactivation of constitutive autophagy results in formation of cytoplasmic protein inclusions and leads to liver injury and neurodegeneration, but the details of abnormalities related to impaired autophagy are largely unknown. Here we used mouse genetic analyses to define the roles of autophagy in the aforementioned events. We report that the ubiquitin- and LC3-binding protein "p62" regulates the formation of protein aggregates and is removed by autophagy. Thus, genetic ablation of *p62* suppressed the appearance of ubiquitin-positive protein aggregates in hepatocytes and neurons, indicating that p62 plays an important role in inclusion body formation. Moreover, loss of *p62* markedly attenuated liver injury caused by autophagy deficiency, whereas it had little effect on neuronal degeneration. Our findings highlight the unexpected role of homeostatic level of p62, which is regulated by autophagy, in controlling intracellular inclusion body formation, and indicate that the pathologic process associated with autophagic deficiency is cell-type specific.

INTRODUCTION

Macroautophagy (hereafter referred to as autophagy) is a highly conserved bulk protein degradation pathway in eukaryotes. In the initial step of this process, the cytoplasmic portions and organelles are engulfed within a double-membrane vesicle called autophagosome, and then the autophagosome fuses with the lysosomes to degrade the sequestered materials by various lysosomal hydrolytic enzymes, followed by generation of amino acids that are recycled for macromolecular synthesis and energy production. Emerging evidence emphasizes the importance of autophagy in various biological and pathological processes, such as cellular remodeling, tumorigenesis, and developmental programs (Levine and Klionsky, 2004).

Recent evidence indicates that in mammalian cells, autophagy serves two physiological purposes. The first is to supply amino acids for cell survival under poor environmental conditions, which is universally known as "adaptive autophagy." Indeed, this type of autophagy is rapidly induced under nutritional deprivation in yeast (Tsukada and Ohsumi, 1993) and in newborn mice (Kuma et al., 2004), serving as a basic survival strategy in all eukaryotes. The second is to degrade proteins in the cell through continuous operation at a low level irrespective of nutritional stress, known as "basal or constitutive autophagy." In the latter pathway, autophagy is responsible for the

turnover of long-lived proteins, disposal of excess (Iwata et al., 2006) or damaged organelles (Elmore et al., 2001), and clearance of aggregate-prone proteins (Fortun et al., 2003; Kamimoto et al., 2006; Ravikumar et al., 2004). Recent genetic studies using mice have highlighted the importance of constitutive autophagy in nondividing cells, such as hepatocytes and neurons, in which loss of autophagy results in severe liver injury and neurodegeneration, respectively (Hara et al., 2006; Komatsu et al., 2005, 2006). Unexpected findings in these studies were that loss of autophagy causes cytoplasmic accumulation of ubiquitin-positive proteinaceous inclusions, together with hepatocytic and neuronal death without expression of proteins with disease-associated mutations (Hara et al., 2006; Komatsu et al., 2005, 2006). However, the underlying mechanism of inclusion body formation in the aforementioned diseases is largely unknown at present.

Using mouse genetics, we report the critical role of the multifunctional protein "p62/A170/SQSTM1" (also known as a signaling adaptor/scaffold protein) in the formation of intracellular ubiquitin-related protein aggregation caused by deficiency in autophagy. We show that autophagic degradation of the "p62" via direct interaction with LC3, a posttranslational modifier essential for autophagosome formation, prevents inclusion body formation. Importantly, our studies uncover the molecular mechanism linking autophagy, p62, and inclusion body formation, which is a cellular hallmark in various pathophysiological conditions, and reveal pathophysiological changes associated with loss of p62 and/or autophagy in hepatocytes and neurons.

RESULTS

Identification of LC3-Interacting Proteins

The microtubule-associated protein 1A/1B *light chain 3* (LC3) is a modifier protein conjugated with phosphatidyl-ethanolamine (PE), analogous to Atg8 in yeast (Ichimura et al., 2000). PE-conjugated LC3 (LC3-II) is localized in the inner and outer membranes of autophagosomes, and the population associated with the inner membrane is degraded after fusion of autophagosomes with lysosomes (Kabeya et al., 2000). To identify protein(s) that could interact with LC3, we employed the proteomic approach as described previously (Komatsu et al., 2004) and then identified a unique protein p62 as one of LC3-interacting proteins, in addition to LC3-modifying enzymes (Ohsumi, 2001) (Table S1). The p62 protein is conserved in metazoa and plants but not in yeasts and can bind a large number of proteins through its multiple protein-protein interaction motifs (Moscat et al., 2006) (Figure S1). This protein mediates diverse signaling pathways including cell stress, survival, and inflammation (Moscat et al., 2006; Wooten et al., 2006).

p62 Is Degraded by Autophagy-Lysosome Pathway

To verify the interaction between LC3 and p62 in vivo, we first carried out immunoprecipitation assay with cultured hepatocytes isolated from green fluorescent protein (GFP)-LC3 transgenic (Tg) mice (GFP-LC3 tg) (Mizushima et al., 2004) and confirmed the coimmunoprecipitation of p62 with GFP-LC3 under both nutrient-rich and -poor conditions (Figure 1A). We also confirmed the coimmunoprecipitation of p62 with endogenous LC3 in wild-type mouse liver (Figure 1B). In addition to the major band, the minor band detected by our p62 antibody was probably a p62 splicing variant product found in the mouse protein database or a partially cleaved product (see also Figures 2, 3, and 4). Moreover, recombinant p62 was pulled down with recombinant GST-LC3 (Figure 1C), indicating direct physical interaction between p62 and LC3. Subsequent binding assays with a series of recombinant p62 mutants indicated that p62 interacts with LC3 through a linker region that connects the N-terminal Zinc finger and the C-terminal *ub*iquitin-associated (UBA) domain of p62 (Figure S1). Immunofluorescence microscopy using hepatocytes isolated from GFP-LC3 Tg mice showed colocalization of large numbers of punctate signal for GFP-LC3 $(84.7\% \pm 10.9\%, \pm SD, n = 21)$ with that for p62 (Figure 1E). When autophagosome formation was induced by nutrient-deprivation, $34.9\% \pm 6.7\%$ $(n = 22)$ of ring-shaped GFP-LC3-positive autophagosomes contained p62 signal, some of which showed partial colocalization (Figure 1F). A similar colocalization pattern was also observed in liver sections of GFP-LC3 Tg starved for 1 day (Figure 1G). The p62-positive and GFP-LC3-negative particles might correspond to late endosomes or lysosomes, as reported previously (Sanchez et al., 1998). Consistent with the notion that some population of LC3-II is degraded in lysosomes (Kabeya et al., 2000), treatment with lysosomal enzyme inhibitors, but not with a proteasomal inhibitor, resulted in the accumulation of LC3-II in primary hepatocytes (Figure 1D). Similarly, lysosomal inhibition resulted in marked accumulation of p62 (Figure 1D). When lysosomal inhibitors were added to cultured hepatocytes, the majority of p62 accumulated around the perinuclear region, where it colocalized with the lysosomal marker LysoTracker (Figure 1H), suggesting the turnover of p62 together with LC3II in lysosomes.

p62 Is a Component of Inclusions in Autophagy-Deficient Hepatocytes

If p62 is degraded by the autophagic-lysosome pathway, autophagy deficiency should result in the accumulation of p62 protein. To test this in vivo, we used the $Atg7^{F/F}$:Mx1 mice, in which *Atg7*, a gene essential for autophagy, can be depleted in the liver by intraperitoneal injections of polyinosinic acid-polycytidylic acid (pIpC) (Figure 2A, left panel) (Komatsu et al., 2005). We observed specific accumulation of p62 protein in *Atg7*-deficient livers (Figures 2A and 2D) without marked induction of p62 mRNA (Figure 2E). Similar to *Atg7* knockout liver, deficiency of *Atg5*, which is essential for autophagosome formation (Mizushima et al., 2001), was also associated with marked accumulation of p62 (Figure S2). These results indicate that p62 turnover is mediated by autophagy. Autophagic
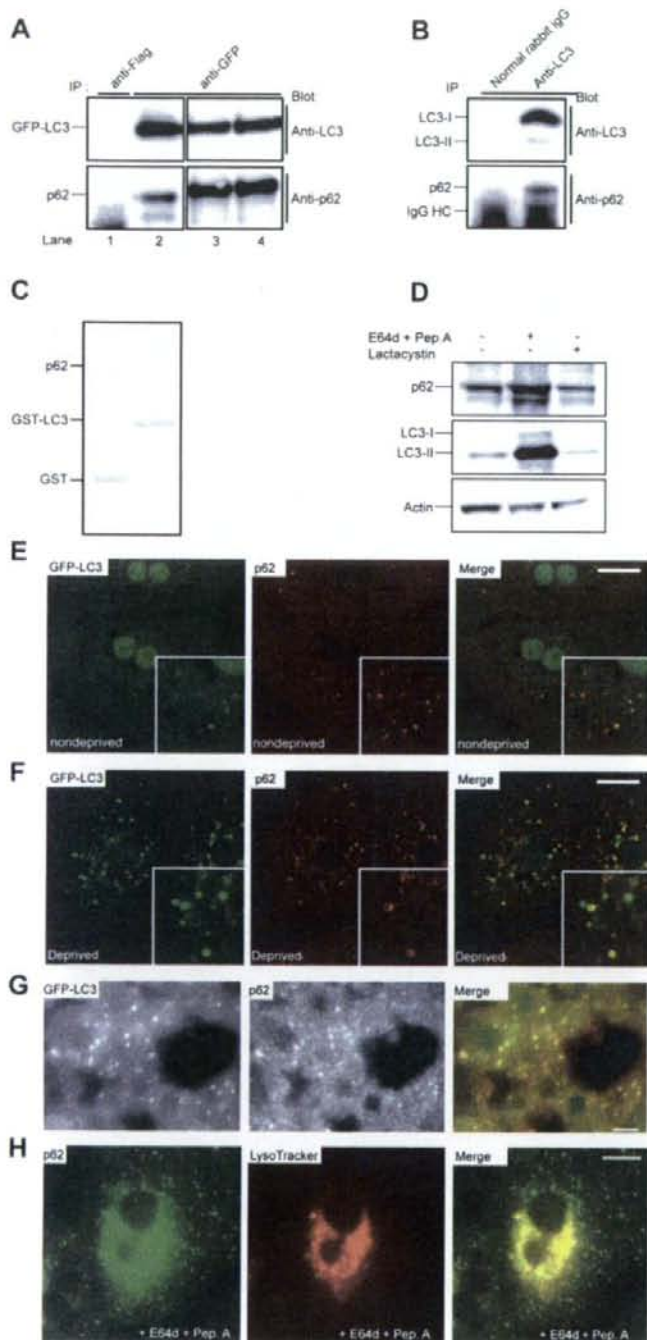
Figure 1. p62 Is Degraded by the Autophagic-Lysosomal Pathway

(A) Interaction of p62 with GFP-LC3. Hepatocytes prepared from GFP-LC3 Tg mice were cultured for 3 hr in Williams' E medium (lanes 1, 2, and 3) or Hank's solution (lane 4). The cell lysates were immunoprecipitated with anti-Flag or GFP antibodies followed by immunoblotting with antibodies against LC3 and p62.

(B) Interaction of p62 with endogenous LC3. Liver lysates from wild-type mice were immunoprecipitated with anti-LC3 antibody or normal rabbit IgG followed by immunoblotting with antibodies against LC3 and p62.

(C) In vitro GST pull-down analysis of purified p62 by recombinant GST or GST-LC3.

(D) Degradation of p62 and LC3. Hepatocytes prepared from wild-type mice were treated with E64d (10 µg/ml) and pepstatin A (10 µg/ml) for 24 hr or lactacystin (10 µM) for 3 hr. The cell lysates were subjected to SDS-PAGE followed by immunoblotting with indicated antibodies. Data shown in (A)–(D) are representative of three separate experiments.

(E, F, and H) Immunofluorescent analysis of primary cultured hepatocytes. Hepatocytes isolated from GFP-LC3 Tg mice were cultured for 3 hr in Williams' E medium (E) and Hank's solution (F) or for 24 hr in Williams' E with E64d and pepstatin A (H) and then immunostained with antibody against p62. Lysosomal inhibitor-treated hepatocytes were stained with the fluorescent acidotropic probe LysoTracker prior to p62 immunostaining (H). Higher magnification views are shown in insets. Bar, 10 µm.

(G) Immunofluorescence analysis of the liver of GFP-LC3 Tg mice. Mice were fasted for 1 day, and then the liver sections were immunostained with anti-p62 antibody. Right panels show merged images. Bar, 10 µm.
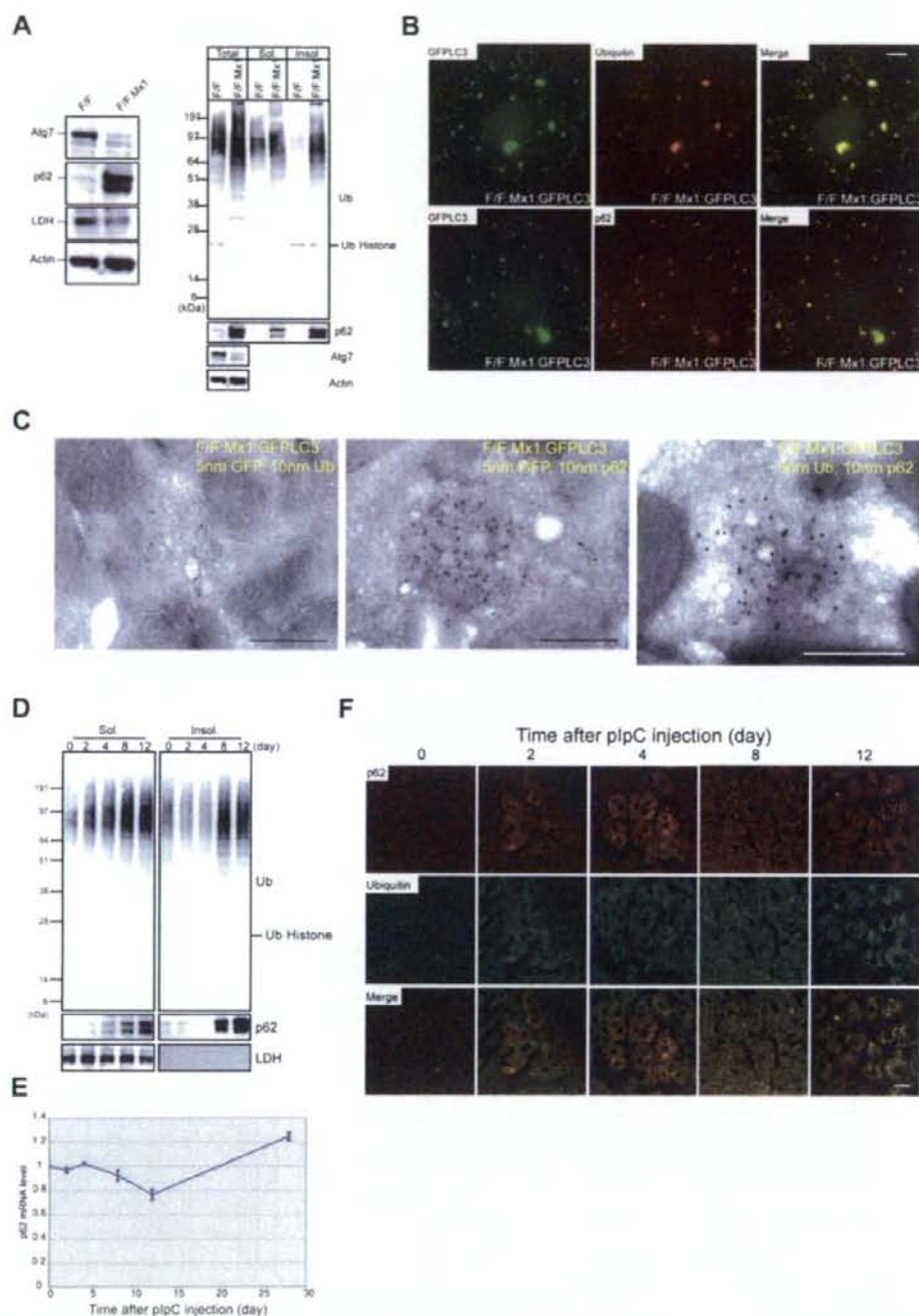
A

B

C

D

E

F

Figure 2. Formation of Ubiquitin- and p62-Positive Inclusions in Autophagy-Deficient Hepatocytes

(A) Accumulation of p62 in *Atg7*-deficient hepatocytes. Left panel shows liver homogenates from *Atg7*$^{F/F}$ and *Atg7*$^{F/F}$:Mx1 mice at 28-day post-plpC injection were subjected to SDS-PAGE followed by immunoblotting with indicated antibodies. Right panel shows liver homogenates were separated

breakdown of p62 appears to occur irrespective of cell type, because a similar observation was recently reported in HeLa, HEK293T, and mouse embryonic fibroblasts (Bjorkoy et al., 2005; Wang et al., 2006).

Interestingly, abundant amounts of p62 were noted in both detergent-soluble and insoluble fractions from Atg7-deficient livers (Figure 2A, right-middle panel), in parallel with accumulation of ubiquitinated proteins in both fractions from Atg7-deficient but not from control livers (Figure 2A, right-top panel) (Komatsu et al., 2005). Subsequently, to investigate the cellular localization of ubiquitin, p62, and LC3 in autophagy-deficient hepatocytes, we generated the $Atg7^{F/F}$:Mx1:GFP-LC3 mice by crossing $Atg7^{F/F}$:Mx1 with GFP-LC3 Tg mice. Immunofluorescence microscopy showed that the Atg7-deficient cultured hepatocytes contained abundant ubiquitin- (Figure 2B, top panels), or p62- (Figure 2B, bottom panels) positive inclusions in the cytoplasm, which were also positive for GFP-LC3. Finally, double immunoelectron microscopy confirmed the colocalization of LC3, ubiquitin, and p62 proteins in the cytoplasmic aggregated structures (Figures 2C and S3). Next, we analyzed the inclusion formation process. Immunoblot analysis revealed that p62 began to accumulate in the detergent-soluble fraction at 4 days and was abundant in both detergent-soluble and -insoluble fractions at 8 days (Figure 2D). In contrast, RT-PCR analysis showed no induction of p62 transcript during this period (Figure 2E). The accumulation pattern of polyubiquitinated proteins essentially matched that of p62 (Figure 2D). Double-immunofluorescence microscopy showed the appearance of ubiquitin- and p62-double-positive dots at 2 days in some $Atg7^{F/F}$:Mx1 hepatocytes (Figure 2F). At later stages, both the number of hepatocytes containing the inclusions and the size of the inclusions increased gradually with time. These results suggest the time-dependent development of inclusions containing both ubiquitin and p62 in autophagy-deficient hepatocytes.

p62 Is a Component of Inclusions in Autophagy-Deficient Neurons

Next, we investigated the behavior of p62 in neuronal-specific autophagy-deficient mice, $Atg7^{F/F}$:Nes mice

(Komatsu et al., 2006). Similar to autophagy-deficient livers, p62 accumulated in the mutant brain without the apparent induction of its mRNA (Figures 3A and 3B), implying a common pathway in p62 turnover across tissues. Furthermore, the p62-positive inclusions were observed immunohistochemically in various brain regions in $Atg7^{F/F}$:Nes mice (Figure S4). Double-immunofluorescence microscopy revealed extensive colocalization of p62 and LC3 (Figure 3C, left panels), or p62 and ubiquitin (Figure 3C, right panels), in numerous inclusions in the cerebral cortex. Immunoelectron microscopy confirmed the localization of p62 in the cytoplasmic aggregated structures (Figures 3D, top panel, and S5). These inclusions also contained ubiquitin (Figures 3D, bottom panel, and S5). Next, we investigated the time course of inclusion formation in the cerebral cortex of $Atg7^{F/F}$:Nes mice from 2 to 28 days after birth. Ubiquitin/p62-double-positive dots began to appear at postnatal day 2 in the cerebral cortex, and they increased in size and number during postnatal development (Figure 3E). Taken together, these results indicate that reduced autophagic activity leads to the formation of ubiquitin- and p62-double positive inclusions in neurons.

Generation of p62-Knockout Mice

To examine the physiological roles of p62 in autophagy, we generated p62-knockout ($p62^{-/-}$) mice (Figure S6). They were born at Mendelian frequency, fertile and lived longer than 1 year (data not shown). Although p62 deficiency was associated with adulthood-onset obesity and diabetes as reported recently (Rodriguez et al., 2006), no apparent abnormality was noted in the p62-deleted liver (Figure S7). Moreover, p62-deficient mice exhibited neither marked neurodegeneration nor inclusion formation in neurons (see Figures 6 and S8). The conversion from LC3-I to LC3-II, induction of GFP-LC3 dots, and the appearance of many autophagosome structures after starvation were similar between the control and p62-deficient hepatocytes (Figures S9A, S9B, and S9C). Furthermore, there was no significant change in the turnover of long-lived protein in the mutant hepatocytes (Figure S9D).

into detergent (0.5% Tx-100)-soluble (Sol.) and insoluble (Insol.) fractions. Each fraction was subjected to SDS-PAGE and analyzed by immunoblotting with indicated antibodies. Data shown are representative of three separate experiments.

(B) Immunofluorescence analysis of cellular localization of ubiquitin, p62, and LC3 in autophagy-deficient hepatocytes. Hepatocytes isolated from $Atg7^{F/F}$:Mx1:GFP-LC3 mice at 14-day post-pIpC injection were immunostained with anti-ubiquitin or p62 antibodies. Right panels show merged images. Bar, 10 μm.

(C) Immunoelectron micrograph showing double labeling of ubiquitin (10 nm colloidal gold particles [cgp]) and GFP (5 nm cgp), p62 (10 nm cgp), and GFP (5 nm cgp), or p62 (10 nm cgp) and ubiquitin (5 nm cgp) in hepatocytes isolated from $Atg7^{F/F}$:Mx1:GFP-LC3 mice at 14-day post-pIpC injection. Bars, 0.5 μm. Magnified images can be seen in Figure S3.

(D) Immunoblotting analyses of ubiquitinated proteins and p62 in $Atg7^{F/F}$:Mx1 mice livers at various time points post-pIpC injection. Each fraction prepared as shown in (A) was subjected to SDS-PAGE and analyzed by immunoblotting with indicated antibodies. Data shown are representative of three separate experiments.

(E) Quantitation of p62 mRNA level in $Atg7^{F/F}$:Mx1 liver by RT-PCR. Total RNAs were prepared from $Atg7^{F/F}$:Mx1 livers at various time points post-pIpC injection, and then cDNA was synthesized from each RNA, followed by real-time PCR analysis. Data are mean ± standard deviation (SD) values of p62 mRNA normalized to the amount in $Atg7^{F/F}$:Mx1 liver at 0 day post-pIpC injection.

(F) Immunohistochemical detection of p62- and ubiquitin-positive inclusions in Atg7-deficient livers. $Atg7^{F/F}$:Mx1 mice were sacrificed at various time points post-pIpC injection, and liver sections were immunostained with anti-ubiquitin and p62 antibodies. Bottom panels show merged images. Bar, 10 μm.